Journal of CO2 Utilization 50 (2021) 101593

Contents lists available at ScienceDirect

Journal of CO2 Utilization

journal homepage: www.elsevier.com/locate/jcou

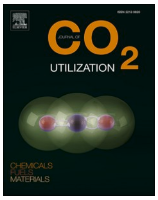

Structure and properties of KNi–hexacyanoferrate Prussian Blue Analogues for efficient CO_2 capture: Host–guest interaction chemistry and dynamics of CO_2 adsorption

Stanislava Andonova [a,*], Sina Sadigh Akbari [b], Ferdi Karadaş [b,c,**], Ivanka Spassova [a], Daniela Paneva [d], Konstantin Hadjiivanov [a]

[a] Institute of General and Inorganic Chemistry, Bulgarian Academy of Sciences, 1113, Sofia, Bulgaria
[b] Chemistry Department, Bilkent University, 06800, Bilkent, Ankara, Turkey
[c] UNAM–National Nanotechnology Center, Bilkent University, 06800, Ankara, Turkey
[d] Institute of Catalysis, Bulgarian Academy of Sciences, 1113, Sofia, Bulgaria

ARTICLE INFO

Keywords:
CO_2 storage adsorbents
Prussian Blue Analogues
Structural distortions
Infrared spectroscopy

ABSTRACT

Potassium Nickel hexacyanoferrate Prussian Blue Analogues (K-NiFe-PBAs) offer an excellent platform for efficient CO_2 capture due to their porous nature and accessible channels. Herein, the effect of Ni:K atomic ratio on the structure and the CO_2 storage capacity was studied by employing K-NiFe-PBAs with Ni:K ratio of ca. 2.5 and 12. The porosity and the isosteric heat of CO_2 adsorption can be modulated and optimized by varying the Ni:K atomic ratio in the PB framework and thus, covering the thermodynamic criterion for easy CO_2capture and release with acceptable energy costs. The synthesized K-NiFe-PBAs containing only trace amounts of K^+ ions (with Ni:K = 12) shows an adsorption capacity (~3.0 mmol g^{-1} CO_2 at 273 K and 100 kPa) comparable to other well established CO_2 adsorbents. *In situ* FTIR spectroscopy was further employed to elucidate the host–guest interaction chemistry and the dynamics of K-NiFe-PBAs within CO_2 and H_2O. The analysis enabled, to the best of our knowledge, is the first FTIR spectroscopic observation of the high sensitivity of the material to structural distortions induced by small changes under water vapor pressure. It was found that H_2O hardly affects CO_2 adsorption and the materials are perspective for CO_2 capture in the presence of water.

1. Introduction

The steady increasing levels of anthropogenic emissions of carbon dioxide (CO_2) into the atmosphere are one of the most significant environmental problems for our society. CO_2 is the most critical greenhouse gas affecting climate change [1–3] and also represents an essential future carbon feedstock. Thus, the control of CO_2 amount is considered a challenging research topic. Many governments are establishing joint efforts [4,5] to encourage the development of new technologies for more efficient CO_2 capture.

Current CO_2 capture technologies comprise the use of porous solid–state materials that have exceptionally high chemical stability, increased CO_2 adsorption capabilities, and fast sorption kinetics to desorb CO_2 under mild conditions. In this context, various porous materials with appropriate structural and chemical properties including zeolites [6–8], carbon [9–11], silica–based materials [12–14], and metal organic frameworks (MOFs) [15–24] have been widely investigated for CO_2 capture.

Prussian blue (PB) is a simple coordination polymer. The iron metal centers in the PB framework can be replaced by various metal ions to form Prussian blue analogues (PBAs). This opens up large possibilities for adjusting their properties. PBAs represent a large family of materials with a general formula $A_{2x}M_{(3\text{-}x)}[M'(CN)_6]_2{\cdot}nH_2O$(A = Li, K, Na, Cs, Rb; M = Cr^{3+}, Mn^{2+},$Fe^{2+/3+}$, $Co^{2+/3+}$, Ni^{2+}, Cu^{2+}, Zn^{2+}, and M' = $Fe^{2+/3+}$, $Co^{2+/3+}$, Cr^{3+}, Mn^{2+}). In a three–dimensional (*3D*) face–centered cubic PB network, the metal ions are connected through cyanide bridging ligands to afford a structure with cavities filled with zeolitic water molecules and alkali cations. These materials recently have drawn growing attention due to their superior performance in various applications [25,26], in alkaline ion batteries [27,28], multivalent ion batteries [29], hydrogen storage [27,30,31], optics [32], magnets [33,34], and electrocatalysis [35–38].

---

* Corresponding author.
** Corresponding author at: Chemistry Department, Bilkent University, 06800, Bilkent, Ankara, Turkey.
E-mail addresses: s.andonova@svr.igic.bas.bg (S. Andonova), karadas@fen.bilkent.edu.tr (F. Karadaş).

https://doi.org/10.1016/j.jcou.2021.101593
Received 5 April 2021; Received in revised form 20 May 2021; Accepted 26 May 2021

In particular, PB and PBAs have shown great potential as efficient adsorbents for CO_2 capture [39–41] due to relatively low regeneration energies, efficient physical adsorption profile, and low–cost precursors. However, a very limited number of articles were published on CO_2 adsorption and separation application that utilizes PBAs. There exist only several reports [39,40,42–46], which mostly focus on the performance aspect rather than providing a detailed spectroscopic account on the nature of the surface species and elucidation of the particular function of various structural components on the CO_2 adsorption mechanism. The high CO_2 adsorption capacity of PBAs has mainly been associated with their high surface area and uniform porosity, which provide easy access to the active sites.

Furthermore, PBAs are highly sensitive to small structural distortions induced by external (mechanical) [47,48] or internal (chemical) pressure [49–51]. Thus, the structure of particular PBAs may undergo specific structural rearrangements, which involve alterations in the geometry of the framework through bending of the $M'-C\equiv N-M$ coordination modes and/or tilting of the $[M(CN)_6]$ units around their crystallographic positions. Based on this, many of the unusual and intriguing properties of these materials were explained considering the slight structural distortions. Therefore, many efforts [47,49,52–54] have been devoted to their experimental detection and quantification. A direct evidence of such small structural distortions is, however, a challenging task, especially when the materials exhibit an intrinsic degree of disorder due to the presence of a variable amount of $[M(CN)_6]$ entities, alkali cations, and water molecules.

In this work, the effect of nickel and potassium content on the structure and the CO_2 adsorption properties of KNi hexacyanoferrate PBAs (K-NiFe-PBAs) was studied by employing samples with different Ni:K atomic ratios of ca. 2.5 and 12, respectively. The samples were synthesized with substantially different porosity and composition containing high– or trace amounts of potassium, as a consequence of charge balance. To study their application as functional materials for efficient CO_2 capture, we performed a series of measurements and analysis of the adsorption isotherms, the CO_2 storage capacity and the isosteric heat of CO_2 adsorption.

The samples were also studied by using a series of complementary characterization experiments including specific surface area, pore volume, pore size distribution, X–ray diffraction (XRD), thermogravimetric and differential thermal (TG–DTA) analysis, Mössbauer spectroscopy, and energy dispersion X–ray spectroscopy in conjunction with scanning electron microscopy (EDX–SEM) to establish a structure & adsorption relationship.

Finally, *in situ* FTIR spectroscopy was employed to elucidate the host–guest interaction chemistry and dynamics of K-NiFe-PBAs with CO_2 and H_2O. The study enabled, to the best of our knowledge, is the first FTIR spectroscopic observation of the high sensitivity of the material to structural distortions induced by small changes under water vapor pressure. Moreover, a drastic effect of potassium on the adsorption properties was established.

2. Experimental

2.1. Synthesis

Two KNi–hexacyanoferrates PBAs with a general formula of $K_xNi_y[Fe(CN)_6]_2\ nH_2O$ were synthesized *via* a co–precipitation method. $K_3[Fe(CN)_6]$ and $Ni(NO_3)_2.6H_2O$ precursors used in the synthesis were purchased from Sigma Aldrich and were of analytical grade purity. In the synthetic protocol, 3 mmol of $K_3[Fe(CN)_6]$ were first dissolved in 50 mL deionized water at room temperature. Then, an aqueous solution of $Ni(NO_3)_2.6H_2O$ (2 or 3 mmol in 50 mL water) were added drop-wise to the above solution. The obtained slurry was stirred continuously for 1 h and left to stand overnight. The resulting precipitates were separated from the mother liquor through centrifugation with filtration and subsequently washed several times with deionized water, and finally dried at 343 K overnight. This method was employed to obtain two compounds with a different Ni:Fe molar ratios of ca. 1:1 and 3:2, respectively. As a consequence, the synthesized K-NiFe-PBAs samples were obtained with a substantially different Ni:K atomic ratios of ca. 2.5 and 12, and a composition containing high– or trace amounts of potassium (Table 1). For brevity, they are denoted in the text as K-rich-NiFe-PBA and K-trace-NiFe-PBA.

2.2. Characterization techniques

2.2.1. Chemical and structural characterization

The elemental composition of the synthesized K-NiFe-PBAs and their molar metal stoichiometry were determined by energy dispersion X–ray spectroscopy in conjunction with scanning electron microscopy (FEI–Quanta 200 FEG ESEM). The EDX data were collected using an electron acceleration voltage of 15 kV and a working distance of 10 mm.

The XRD patterns were obtained with a Rigaku diffractometer, equipped with a Miniflex goniometer and an X–ray source with Cu Kα radiation, at $\lambda = 1.5418$ A, 45 kV, and 40 mA. Diffraction patterns of the samples were recorded in 2θ range between 5 and 80° with a step size of $0.04^\circ\ s^{-1}$. The patterns were assigned using Joint Committee on Powder Diffraction Standards (JCPDS) cards supplied by the International Centre for Diffraction Database (ICDD). The average particle size (D_{av}) was determined using the Scherer equation of the three most intensive diffraction signals.

The powder samples were degassed at 363 K for 24 h prior to N_2 adsorption–desorption isotherms with a Quantachrome Autosorb IQ–C–MP–AG–AG (USA) analyzer. The analysis was performed using nitrogen adsorption data within the relative equilibrium pressure interval of 0.00–1.00 P/P_0. The Brunauer–Emmett–Teller (BET) specific surface areas (S_{BET}, $m^2\ g^{-1}$) were calculated using the BET method, while the total pore volume (V_p, $cm^3\ g^{-1}$) was estimated in accordance with the Gurvich rule at a relative pressure ~0.99. The micropore volume (V_{mi}, $cm^3\ g^{-1}$), the specific surface area of the micropores (S_{mi}, $m^2\ g^{-1}$) and the external specific surface area (S_{ext}, $m^2\ g^{-1}$) were evaluated by the V–t-method [55]. The accuracy of the measurements was established using the t-plots, presented in Fig. S1, *Supplementary Information*. Additionally, the pore size distribution by the Barrett–Joyner–Halenda method and the micropore distribution by the Dubinin–Astakhov method were estimated.

The thermal stability and dehydration temperature of the synthesized materials were studied *via* thermogravimetric and differential thermal analysis by using a Setaram Labsysis Evo 1600 instrument. The temperature–dependent changes in the heat flow (HF, mW) in parallel with the TG curves were reordered from the start of the heating at room temperature to 773 K with a rate of 10 K min^{-1} under an N_2 flow of 20 mL min^{-1}.

Mössbauer spectroscopic measurements were performed at room temperature with an electromechanical spectrometer (Wissenschaftliche Elektronik GMBN, Germany) working in a constant acceleration mode and using a $^{57}Co/Rh$ source. Calibration spectra were recorded by using a standard α–Fe. WinNormos for Igor Pro software for the quantitative evaluation of the spectral parameters (least–squares fitting to Lorentzian peaks) is used. All spectra were fitted using an iterative least squares minimization algorithm and Lorentzian line shapes to obtain the parameters of the hyperfine interaction: isomer shift (IS, mm s^{-1}); quadruple splitting (QS, mm s^{-1}), full width at half maximum (FWHM mm s^{-1}) and relative weight of the partial components (G, %). The fitting procedure was considered as optimal, in case when there is a high convergence between the experimental and theoretical (simulated) spectra (sum of Lorentz lines) at an optimal confidence interval.

2.2.2. Volumetric and breakthrough CO_2 adsorption studies

The CO_2 adsorption isotherms were recorded at two different temperatures, 273 K and 286 K, using a static volumetric Quantachrome NOVA 1200e (USA) analyzer. Prior to the measurements, the samples

Table 1
Chemical composition and main textural characteristics of the K-NiFe-PBAs samples.

Samples	Chemical composition*	Ni/K ratio	S_{BET}** $m^2\ g^{-1}$	S_{mi}** $m^2\ g^{-1}$	S_{ext}** $m^2\ g^{-1}$	V_p** $cm^3\ g^{-1}$	V_{mi}** $cm^3\ g^{-1}$	D_{av}*** nm
K-rich-NiFe-PBA	$K_{1.04+y}Ni_{2.48}[Fe^{II}_yFe^{III}_{1-y}(CN)_6]_2 \square nH_2O$	2.5	72	14	58	0.14	0.01	22.3
K-trace-NiFe-PBA	$K_{0.24+y}Ni_{2.88}[Fe^{II}_yFe^{III}_{1-y}(CN)_6]_2 \square nH_2O$	12	110	10	100	0.31	0.01	17.6

* Metal molar ratio determined *via* EDS–SEM; the □ symbol represents the $[Fe(CN)_6]^{3-}$ vacancies, generated together with the interstitial cations to produce charge balance in the framework. The presence of Fe^{III} and Fe^{II} ions and their ratio was determined by Mössbauer spectroscopy.

** S_{BET} – Specific surface area; S_{mi} – Surface area of the micropore structure; S_{ext} – External surface area; V_p – Total pore volume; V_{mi} – Pore volume of the micropores, determined from the N_2 adsorption isotherms.

*** Average particle size (D_{av}) determined by XRD using the Scherer equation of the three most intense diffraction signals.

were degassed at 363 K under vacuum for 24 h. After that, the samples were exposed to CO_2 at different temperatures within the relative equilibrium pressure interval of 0.00–1.00 P/P_0 (0–100 kPa).

The isosteric heat of CO_2 adsorption (Q_{st}, kJ mol^{-1}) was calculated using the Clausius–Clapeyron Eq. (1):

$$\ln\left(\frac{P_2}{P_1}\right) = -\frac{Q_{st}}{RT_1T_2}\left(\frac{1}{T_2}-\frac{1}{T_1}\right) \tag{1}$$

where T is the temperature, R, the universal gas constant and P, the pressure.

The experimental set–up used for the breakthrough analysis of CO_2 adsorption under dynamic conditions comprises a vertical quartz tube reactor mounted in an electric furnace, part of the assembly of CATLAB (Hiden Analytical) instrument. Prior to each measurement, the samples (approximately 0.1 g of powder sample) were first degassed under a flow of Ar at 363 K for 24 h. Then, the temperature was decreased to the lowest possible at 313 K and the samples were exposed to 15 % CO_2/Ar for 20 min. In all experiments, the total gas flow rate was held constant at 20 mL min^{-1}. The inlet gas composition was controlled by using a system of individual mass flow controllers (Bronkhorst Hi–Tech) and the effluent from the outlet gas was monitored and analyzed on–line using a Hiden HPR 20 quadrupole mass spectrometer (MS) equipped with a heated capillary probe connected directly to the exit of the reactor. The breakthrough analysis (the first evidence of CO_2 in the outlet gas) was performed by recording the MS signals with mass to charge ratio (m/e) equal to 18, 28, and 44 in pressure vs. time mode. The total CO_2 stored (mmol g^{-1}) during the adsorption was calculated by using Eq. (2):

$$\left[CO_{2,ads}\right] = \left(CO_{2,in}\right)t_A - \left(CO_{2,out}\right)t_A \tag{2}$$

$(CO_2,in)t_A$ is the total integrated CO_2 concentration at the reactor inlet during the adsorption period (C_0, mmol g^{-1}), $(CO_2,out)t_A$ is the total integrated CO_2 concentration at the reactor outlet during the adsorption period (C, mmol g^{-1}) and t_A is the length of the adsorption period (min) until the saturation point when the system reaches a steady–state level.

2.2.3. *In situ FTIR spectroscopic adsorption studies*

The FTIR spectroscopic measurements were carried out in transmission mode using Nicolet Avatar 6700 FTIR spectrometer equipped with a Hg–Cd–Te (MCT) detector. The experiments were performed in a batch-type IR cell equipped with optically polished CaF_2 windows allowing data acquisition at low (100 K) or ambient temperatures. The cell was directly connected to a vacuum–adsorption apparatus with a residual pressure lower than 4×10^{-7} kPa. For the FTIR experiments, samples spread onto KBr pellets (ca.10 mg cm^{-2}) were used. They were prepared by pressing the sample powders onto the KBr pellet at a pressure of ~0.5 Tonn cm^{-2}, applied for 1–2 min. Then, the pellets were placed inside the IR cell using a custom–made mobile sample holder allowing insertion of the sample in the middle of the heated zone of the IR cell. Thus, the spectra were registered *in–situ* after each thermal treatment of the sample at different temperatures and atmospheres. Each FTIR spectrum was acquired within the 4000–800 cm^{-1} spectral region by accumulating 64 scans at a spectral resolution of 2 cm^{-1}. The background and gas phase corrections were performed using the OMNIC software.

The samples were analyzed in non-activated (as-prepared), activated (dehydrated) and hydrated (pre-adsorbed with 0.5 kPa H_2O and then evacuated at RT) forms. The activation was performed by heating the pellets at 363 K under vacuum for 1 h to a residual pressure of $\sim 4 \times 10^{-7}$ kPa. The FTIR investigations were performed after adsorption of CO_2, and/or H_2O–vapor on the samples at RT. Carbon dioxide (CO_2, 99.998 % purity) was supplied by Messer. FTIR of low-temperature (100 K) ^{13}CO (ISOTEC, >99.9 % purity) and $^{13}C^{18}O$ (Cambridge Isotope Lab., Inc., >99.9 % purity) adsorption were also performed. Prior each experiment, carbon monoxide was purified by passing through a liquid nitrogen trap.

3. Results and discussion

3.1. *Preliminary structural and textural characterization*

3.1.1. *Chemical composition and structural analysis via EDX–SEM and XRD*

The synthesis method, described in the experimental section, is commonly employed to prepare PBAs [39,56,57] with controlled compositions and morphologies. This can also be confirmed in the current study where the final composition of both prepared materials is almost identical to that pre–set in the synthesis with a Ni:Fe molar ratio, ranging from ~1:1 to ~3:2. As a consequence of charge balance, the synthesized K-NiFe-PBAs samples were obtained with a substantially different Ni:K atomic ratios of ca. 2.5 and 12, respectively, and composition containing rich- or trace amounts of potassium while the (½K + Ni):Fe ratio was kept constant. The different stoichiometry between the samples was firstly evident from the color change from dark green to light brown with increasing the Ni:K ratio and thus, lowering K–content (x = 1.04 →0.24) (Table 1) on the basis of charge–balance. Table 1 shows the chemical composition, which is estimated based on EDX–SEM analysis (Figs. S2 and S3, *Supplementary Information*). In addition, the Table presents the main textural parameters determined based on the measurements of N_2 adsorption at 77 K.

The crystalline structures of the obtained solid powdered materials were determined by X–ray diffraction. The XRD patterns of both K-NiFe-PBAs samples shown in Fig. S4 (a and b, *Supplementary Information*), exhibit strongly pronounced diffraction peaks characteristic of a cubic crystal structure of Fm3m symmetry [58–60], which is typical of PBAs. The high intensity of the diffraction peaks and the absence of any baseline drift reveal the high crystallinity of the samples with only minor impurities, if any. A more detailed analysis of the XRD data shows, however, that although no shift is observed, the primary diffraction signal (200) is considerably broadened and appeared with reduced intensity in the pattern of K-trace-NiFe-PBA compared to K-rich-NiFe-PBA (Fig. S4(B)). Similar changes in the FWHM were also registered for the other intense reflections (220, 400, and 420), suggesting the generation of materials with different crystallinity due to the different Ni:K ratios. The three most intense diffraction signals were used to determine the average particle size (D_{av}, nm) using the Scherrer equation. The results presented in Table 1 confirm that the particle size decreases from 22.3 nm to 17.6 nm once Ni:K ratio increased.

3.1.2. N_2 adsorption and desorption studies

N_2 adsorption/desorption isotherms reveal that K-trace-NiFe-PBA exhibits a porous structure with a much more developed external specific surface area (~100 m^2 g^{-1}) and a total pore volume (~ 0.31 cm^3 g^{-1}) as compared to K-rich-NiFe-PBA (S_{ext} ~ 58 m^2 g^{-1} and V_p~ 0.14 cm^3 g^{-1}) (Table 1). The adsorption profiles of both samples transform from a type I isotherm to a type IV one at $p/p_0 \sim 0.5$, which is typical of materials [61] with a mixed micro– and mesoporous structure (Fig. 1). The adsorption initially proceeds slowly at low relative pressures ($p/p_0 \leq 0.5$) to form a type I isotherm where the micropore filling occurs. In the intermediate region, $p/p_0 \sim 0.5 – 0.95$, the adsorption and desorption branches do not coincide and transform to a type IV isotherm with a wide H1–shaped hysteresis. The existence of hysteresis is typical of mesoporous adsorbents where phase changes such as a pore condensation and/or a multilayer adsorption occur. It is visible in Fig. 1A (isotherm b) that the total amount of N_2 adsorbed on K-trace-NiFe-PBA is at least two times larger than that on K-trace-NiFe-PBA (isotherm a). Particularly for K-rich-NiFe-PBA, the values are considerably reduced in the whole range of relative pressures, which could be attributed to the presence of larger cavities and thus, a more accessible and opened pore structure in K-trace-NiFe-PBA compared to K-rich-NiFe-PBA. Pore size distribution profiles presented in Fig. 1B also support this thesis. The three–modal shape of the pore size distribution of both samples with characteristic features indicates the presence of both micro- and meso–pores.

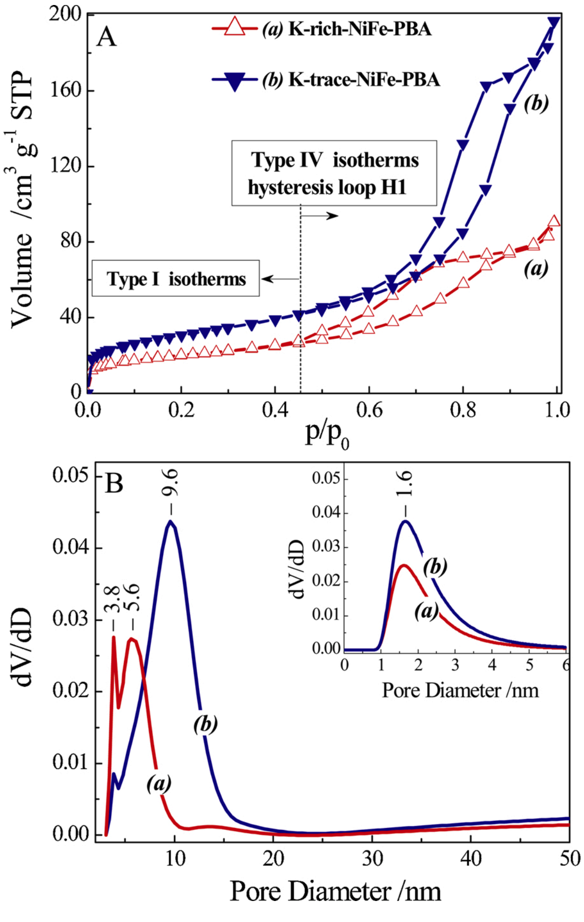

Fig. 1. Panel A. Experimental isotherms of adsorption and desorption of N_2 at 77 K and Panel B. Pore size distribution – meso– and micropores (inset): (a) K-rich-NiFe-PBA and (b) K-trace-NiFe-PBA.

K-trace-NiFe-PBA framework mainly consists of mesoporous channels with larger dimensions (peak with maxima observed at ~9.6 nm, profile b) compared to K-rich-NiFe-PBA (peaks at ~3.8 and ~5.6 nm, profile a). These results clearly show that the porosity of the cyanide KNiFe-PBAs framework correlates with the concentration of alkali K^+ ions and it can readily be adjusted by varying the Ni:K atomic ratio. Thus, in the case of K-rich-NiFe-PBA, the higher alkali content dictates the formation a fully occupied cubic framework enclosing much smaller cavities. In contrast, with the K-trace-NiFe-PBA the alkali ions occupancy is much lower and this creates larger cavities in the framework.

The cage-like structure of both K-NiFe-PBAs systems is composed of cavities between the contiguous nanoparticles, thus forming a system of mesoporous channels with a diameter which varies between 3.8 and 9.6 nm. The narrow porous volume distribution of about 1.6 nm in the pore size is attributed [62,63] to the nanoparticles that exhibit certain microporosity. The porous nature of the materials can be explained with the presence of vacancies in the cubic crystal structure - gaps in the lattice that correspond to missing hexacyanoferrate $[Fe(CN)_6]^{3-}$ ions which form pores in the framework. This is consistent with many fundamental studies [64,65] where it is shown that the actual PBAs crystal structures contain vacancies corresponding to absent hexacyanometallate $[M'(CN)_6]^{3-/4-}$ units. Their concentration and networking ordering control the porosity and the pathways through which the PBAs are able to reversibly transport ions or small molecules [64]. Thus, the differences in the surface area and pore volume of the samples is likely due to a combination of different factors including the concentration of the vacancies, the amounts of potassium ions inserted into the structure, interparticle spacing and internal voids. This could be an indication that in the case of K-trace-NiFe-PBA which has a more developed mesoporous structure the number of the vacancies generated in the absence of any significant amounts of interstitial K^+ cations is considerably higher compared to that of K-rich-NiFe-PBA.

3.2. Thermal stability and degree of hydration determined via thermogravimetric analysis

The thermal stability and dehydration temperature of the compounds were determined *via* TG–DTA analysis. The temperature–dependent changes in the heat flow (HF, mW) in parallel with the TG curves are presented in Fig. S5(A) and S5(B) (*Supplementary Information*), respectively.

The analysis reveals that the profiles of both samples follow similar trends in the evolution of the HF and the weight–loss, which occur in three steps. Similar to the thermal behavior of many other PBAs reported in the literature [66], the first two steps take place almost simultaneously and they correspond to the release of the crystal water in the cavities of the framework and the water molecules coordinated to unsaturated metal sites. In parallel with the TG curves, the changes in the HF were registered in the whole range of temperatures (308–723 K) as endothermic signals with a maximum at ~400 K with a shoulder at ~363 K caused by the heat consumed during the water desorption process. The sample weight loss corresponding to the second step for both samples was found to be ~16.7 % for K-rich-NiFe-PBA and ~18.3 % for K-trace-NiFe-PBA.

The third final stage above 450 K is attributed to the gradual endothermic decomposition and destruction of the cyanide framework. It should be noted that the maximum temperature required for water removal is almost the same for both samples. The changes in the HF were, however, found to be strongly affected by the water content. The HF signal intensity increases notably during the endothermic process of dehydration of K-trace-NiFe-PBA compared to that of K-rich-NiFe-PBA (Fig. S5). This trend indicates that the water content increases as the Ni/K atomic ratio increases, as expected. It should be noted that the alkali metal ions, which reside in the tetrahedral holes of the cubic unit cell, limit the accessibility of the microchannels for water molecules. Therefore, the higher number of water molecules in K-trace-NiFe-PBA can also be attributed to the lower number of potassium content ($x = 0.24$) compared to K-rich-NiFe-PBA ($x = 1.04$).

3.3. Mössbauer spectroscopic analysis of iron in hydrated NiFe-PBAs

Local electronic state of iron (*i.e.*, the oxidation and the spin state of the Fe ions) in K-NiFe-PBAs was further elucidated with Mössbauer spectroscopy. The spectra reordered at room temperature for both samples in hydrated (non-activated) forms are presented in Fig. 2. The main spectral parameters are determined using an iterative least squares minimization algorithm and Lorentzian line shapes (Table 2).

The applied spectral fitting clearly reveals a combination of two components in both compounds: a quadrupole doublet (denoted in blue as Db1) and a singlet (in red, S2), indicating that both frameworks exhibit mixed–valence Fe(III)/Fe(II) structure. The values of the isomer shift and the quadrupole splitting of the doublets for both samples (Table 2) are typical of the hexacyanoferrate(III) anion [67,68] in a Prussian blue structure and refer to the presence of Fe(III) ions in their low–spin states (t_{2g}^{5}).The singlet–line component with its parameters of the hyperfine interaction also reveals the presence of Fe(II) ions [58,66,68] in their low–spin states (t_{2g}^{6}) due to strongly electron donating cyanide ligands.

It can also be seen that the spectra of the quadrupole doublet are dominant for both samples, which indicates that both compounds contain mostly low–spin Fe(III) ions with small amounts of low–spin Fe (II) ions. Furthermore, the experimentally obtained spectrum of K-rich-NiFe-PBA (Fig. 2A) has a more asymmetric shape compared to that of K-trace-NiFe-PBA (Fig. 2B) since the higher–energy component of the doublet (Db1) is more intense than the lower–energy one. The intensity of the singlet–line component (areas under the S2 spectrum line) increases compared to the doublet one. In contrast to the K-rich-NiFe-PBA, the doublet spectrum of K-trace-NiFe-PBA becomes more symmetrical and its intensity increases compared to the singlet one. This change in the symmetry of the Mössbauer spectra indicates that the quadrupole doublet of Fe(III) is dominant in both samples and the samples are characterized by a different Fe(III)/Fe(II) ratio. As presented in Table 2, the analysis of the relative weight of the partial components (G, %) shows that ~24 % of the total iron into the K-rich-NiFe-PBA structure was in the Fe(II) state while it is ~16 % for K-trace-NiFe-PBA.

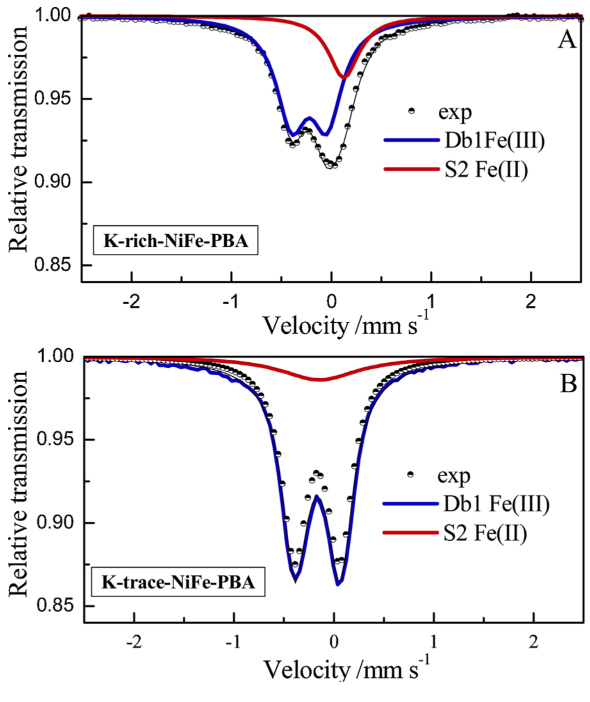

Fig. 2. Experimentally obtained and simulated (theoretically calculated) Mössbauer spectra of the samples in hydrated (non-activated) form: Panel A. K-rich-NiFe-PBA; Panel B. K-trace-NiFe-PBA.

Table 2
Main spectral parameters (least–squares fitting to Lorentzian peaks) determined from the Mössbauer spectra reordered at room temperature for K-NiFe-PBAs in hydrated form.

Samples	Components	IS *mm s^{-1}*	QS *mm s^{-1}*	FWHM *mm s^{-1}*	G *%*
K-rich-NiFe-PBA	Db1 - Fe(III)	−0.21	0.39	0.37	76
	S2- Fe(II)	0.12	0.00	0.37	24
K-trace-NiFe-PBA	Db1 - Fe(III)	−0.17	0.45	0.30	84
	S2 - Fe(II)	−0.08	0.00	0.96	16

3.4. CO_2 adsorption behaviour

The CO_2 adsorption isotherms of K-NiFe-PBAs were recorded at two different temperatures (273 K and 286 K) to evaluate the CO_2 storage capacity and the isosteric heat of CO_2 adsorption ($Q_{st,}$ kJ mol^{-1}). The results from the measurements are presented in Fig. 3A while the surface coverage–dependent changes in the enthalpy upon the adsorption are shown in Fig. 3B. In addition, the breakthrough curves of 15 % CO_2 in the feed gas obtained at 313 K under dynamic conditions are displayed in Fig. 3C.

As observed from Fig. 3A, both isotherms of K-trace-NiFe-PBA are characterized by a steeper rise compared to those of K-rich-NiFe-PBA and the amount of CO_2 adsorbed is significantly higher in the whole range of pressures for the adsorbent with the trace amounts of potassium. Furthermore, none of the measured isotherms of K-trace-NiFe-PBA reach a plateau of steady–state, which indicates that a maximum saturation is not achieved yet and the mesopores are not completely filled at these conditions. Thus, the CO_2 adsorbed amount could be enhanced further at pressures higher than 100 kPa. A remarkable uptake of ~2.6 mmol $g^{-1}CO_2$ is obtained for K-trace-NiFe-PBA, which is comparable to other well established CO_2 adsorbents, *e.g.*, zeolite 13X (~4.5 mmol g^{-1}) [69], activated carbon (AC) (~2.9 mmol g^{-1}) [70], and different MOFs (MIL-101 ~3.6 mmol g^{-1}; MOF-5 ~2.1 mmol g^{-1}; ZIF ~3.5 mmol g^{-1}) [16,71,72], all are measured at ambient temperatures and 100 kPa. A more systemized information about the CO_2 storage capacity, the nature of the adsorption sites and their distribution on the MOF-based materials can be seen into several recently published review papers [17,73].

Since the adsorption capacity decreases with increasing the temperature, the sorption process is an exothermic and mostly controlled by physisorption. However, the effect is more discernible for K-rich-NiFe-PBA while K-trace-NiFe-PBA is characterized with no significant changes in the adsorption capacity at 273 and 287 K (Fig. 3A). This profile is in good agreement with the porous nature of the studied samples since K-trace-NiFe-PBA has a more developed mesoporous structure, which results in stronger attractive electrostatic interactions between the CO_2 molecules adsorbed inside the larger channels.

The proposed explanation for the enhanced adsorption in K-trace-NiFe-PBA is also in a reasonably good agreement with the data presented in Fig. 3B, which displays the surface coverage–dependent changes in the CO_2 adsorption enthalpy. The heat released during the storage process for K-rich-NiFe-PBA is considerably higher compared to that of K-trace-NiFe-PBA, indicating that the thermodynamic characteristic of the interaction of the adsorbents with CO_2 can be modulated and optimized *via* increasing the Ni:K ratio. At low CO_2 coverages, the Q_{st} values of K-rich-NiFe-PBA and K-trace-NiFe-PBA were estimated at the same amount of CO_2 adsorbed (~ 0.32 mmol g^{-1}) to be 56.2 and 23.8 kJ mol^{-1}, respectively.

This remarkable difference can be rationalized assuming the existence of a fraction of very energetic sites for CO_2 adsorption on K-rich-NiFe-PBA. Evidently, this phenomenon should be associated with the

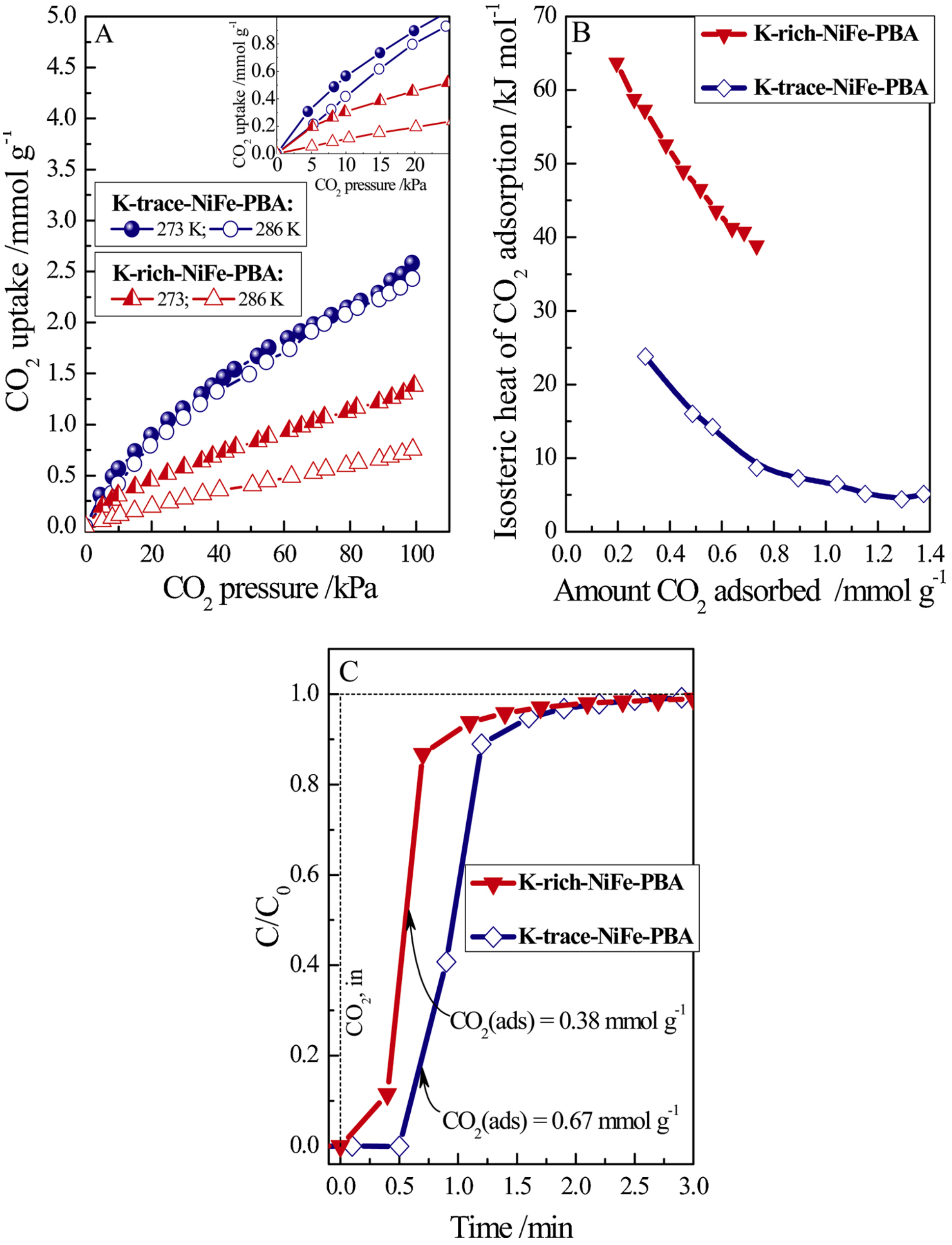

Fig. 3. Panel A. Adsorption isotherms of CO_2 at 273 K and 286 K within the relative pressure interval of 0–100 kPa; Inset: Zoom showing the isotherms at pressure up to 25 kPa. Panel B. Isosteric heat of CO_2 adsorption of K-NiFe-PBAs samples, activated at 363 K for 24 h; Panel C. Breakthrough curves of 15 % CO_2 in feed gas obtained at 313 K under dynamic conditions; (C_0, C, mmol g^{-1} are the CO_2 concentrations at the reactor inlet/outlet).

higher content of potassium. The observation is also discussed below, and here we note that it was recently reported [74] that K^+ cations effectively embedded in the porous MOFs can act synergistically to generate highly specific binding sites for trapping CO_2 and can enhance the selective sorption and isosteric heat. Fig. 3B also shows that with both samples the isosteric heat of adsorption gradually diminishes with the surface coverage increase. This indicates that the heterogeneity of both surfaces affords a multilayer CO_2 adsorption process and thus, a gradual decrease in the interaction between the adsorbate CO_2 molecules and the surface. The Q_{st} values for K-trace-NiFe-PBA were estimated to be of only around 2–3 kJ mol^{-1}, which reveals that at high coverages the CO_2 adsorption occurs mostly physically and the material can easy capture and release CO_2 with acceptable energy costs.

The results were also in good agreement with the data presented in Fig. 3C, which displays the CO_2 uptake behavior under dynamic conditions at 313 K. In these experiments, the breakthrough profile of K-rich-NiFe-PBA is detected almost immediately when the exposure is initiated while that of K-trace-NiFe-PBA is delayed. Particularly, K-trace-NiFe-PBA reaches a full saturation of ~ 0.7 mmol g^{-1} CO_2 within ~ 2 min, which is about two times higher than the adsorption capacity of K-rich-NiFe-PBA (~0.38 mmol g^{-1} CO_2). This is consistent with the presence of a greater concentration of framework vacancies within the K-trace-NiFe-PBA compared to K-rich-NiFe-PBA. Thus, the enhanced CO_2 capture indicates that the cavity size within the mesoporous structure and the surface area play important roles in the adsorption efficiency of Prussian blue systems.

3.5. *In situ FTIR spectroscopic adsorption studies*

Further insight regarding the nature of the surface species and the host–guest interaction chemistry and dynamics of K-NiFe-PBAs with CO_2 and H_2O was obtained *via in–situ* adsorption FTIR analysis.

3.5.1. *FTIR spectra of the as-prepared and dehydrated K-NiFe-PBAs*

The FTIR spectra of the as-prepared (non-activated) K-NiFe-PBAs samples (a, c) and those evacuated at 363 K (b, d) are presented in Fig. 4. For convenience, the insets of the Figure show the spectra (b, d) in the ν(O−H) (left) and ν(C≡N) (right) stretching regions.

The spectra (a and c) of both as-prepared K-NiFe-PBAs materials reveal similar IR features consistent with earlier reports [58,60,66,75–81]. The non-activated samples (exposed to air) contain a distinct band at ca. 3645 cm^{-1} and a broad feature extended from 3800 to 3200 cm^{-1} and centered around 3400 cm^{-1}. All these bands are attributed to the OH stretching modes of water molecules on the surface of PB particles. The sharper band at around 3645 cm^{-1} corresponds to isolated OH groups attached to PB structures or water molecules having an isolated OH moiety. The broad band is due to H–bonded OH groups from adsorbed water and probably H–bonded OH groups. Two IR bands at ca.1610 cm^{-1} and 1654 cm^{-1} correspond the δ(H−O−H) bending modes, which indicates the presence of two types of adsorbed water molecules: i) water in the cavities and ii) coordinated water molecules to complete the coordination sphere of the unsaturated nickel or iron ions. An additional feature at ca. 1415 cm^{-1} is also registered, which suggests the presence of small amounts of nitrates [82] coordinated to the alkali ions originating from the preparation technique. The higher intensity of the band in the spectrum (a) is consistent with the higher potassium content.

Additional information can be obtained by the analysis of the ν(CN) stretching region since the CN stretching modes are sensitive to the coordination and the oxidation state of the metal ion [83]. The $[Fe(CN)_6]^{3-}$ ion in an aqueous solution shows ν(CN) modes at 2080 cm^{-1}. In particular, for K-NiFe PBAs, the Fe(III)−CN−Ni(II) coordination mode exhibits a CN stretch at 2165 cm^{-1}, while it is at 2095–2085 cm^{-1} for Fe(II)−CN−Ni(II) [58,60,66,78–81]. The difference is due to the enhanced σ–donating and reduced π–accepting ability of cyanide towards Fe(III) ions compared to Fe(II) ones.

Analysis of the spectra of our samples indicates that both samples contain two prominent bands in the cyanide region, with maxima located at 2163 and 2097−2089 cm^{-1} (Fig. 4, spectra a,c). These bands are unambiguously associated with Fe(III)−CN−Ni(II) and Fe(II)−CN−Ni(II) moieties, respectively (see also Fig. S6, *Supplementary Information*). Thus, the IR spectra demonstrated that the samples contain both Fe(III) and Fe (II) species, which is consistent with the Mössbauer spectroscopic data. Moreover, the relative intensity of the lower–frequency band associated with Fe(II) is higher with the sample having a higher fraction of Fe(II), according to the Mössbauer results. Note, however, that the extinction coefficient of the bands at 2097–2089 cm^{-1} is expected to be higher compared to the Fe(III)–related bands, due to enhanced back π–donation. Therefore, the high intensity of the bands at 2097–2089 cm^{-1} cannot be related to a higher concentration of Fe(II) than of Fe(III) cations.

A careful inspection of the spectra reveals additional features. A shoulder at 2052 cm^{-1} is well discernible with K-rich-NiFe-PBA while a shoulder at a lower frequency and with a lower intensity is detected with K-trace-NiFe-PBA at around 2033 cm^{-1}. The features are assigned to the presence of terminal cyanide Fe(II)−C≡N− ligands as the difference in the intensities is consistent with the stoichiometry of the samples having different Fe(III)/Fe(II) ratio. In addition, there is a weak band at 1945 cm^{-1} which is assigned to NO coordinated to the iron species [84] and resulting from CN oxidation. This indicates that the synthesized K-NiFe-PBA compounds containing ferrous complexes may undergo partial oxidation when exposed in air.

Once samples are dehydrated, the ν(OH) band at 3643 cm^{-1} and the broad signal at ca. 3408 cm^{-1} disappears and new small features at 3685, 3657, and 3628 cm^{-1} developed instead (see the inset on the left). Since the modes at 3685 and 3657 cm^{-1} blue–shift when H–bonding is almost eliminated they could be attributed to the ν(OH) stretching vibrations of isolated OH groups that are coordinated to Ni(II) sites. The water molecules and the residual nitrates are easily removed from K-trace-NiFe-PBA. The bands at 1608, 1654, 1412, and 1323 cm^{-1} in spectrum (d) almost entirely vanished after evacuation while the bands in the spectrum (b) of K-rich-NiFe-PBA remained almost unaffected probably due to diffusion limitations within the narrow pores.

Importantly, the prominent bands at ca. 2163 and 2097 cm^{-1} are slightly affected by water. As observed from the inset on right of Fig. 4, evacuation leads to broadening and a blue shift of the bands. The effect is more discernible with K-trace-NiFe-PBA (spectra c and d), where water molecules in the structure are almost completely removed. The sensitivity of the ν(C≡N) stretching modes of K-trace-NiFe-PBA to the coordination mode suggests that the structure may undergo rearrangements and alterations in the geometry of the framework upon dehydration. Different PBAs have been reported to be sensitive to small structural distortions induced by external (mechanical) [47,48,52] or internal (chemical) pressure [49–51,54]. A combination of different techniques was used to understand and explain this behavior while the host–guest

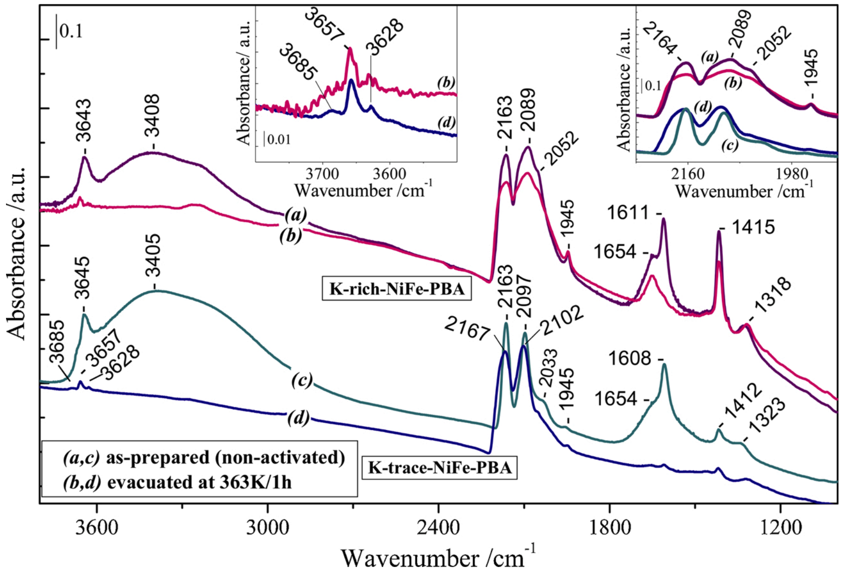

Fig. 4. FTIR background spectra of the as-prepared (non-activated) K-NiFe-PBAs samples (a, c) and those activated after evacuation at 363 K for 1 h (b, d). The insets of the figure show the spectra in the ν(O−H) (left) and ν(C≡N) (right) stretching region.

interaction chemistry and dynamics of K-NiFe-PBAs within H_2O and CO_2 have not been addressed previously. Thus, further information was obtained using *in–situ* adsorption FTIR analysis.

To summarize the data, the structure of both as-synthesized K-NiFe-PBAs, of nominal composition $K_{x+y}Ni^{II}[Fe^{II}{}_{y}Fe^{III}{}_{1\text{-}y}(CN)_6]\ \square\ n{\cdot}H_2O$ can be described including $Ni(NC)_6$ and $M(CN)_6$ entities ($M{=}Fe^{III}$, Fe^{II}) that are linked by sharing of cyanide bridging groups and forming a three-dimensional cubic framework of linearly repeating −NC−M−CN−Ni−NC units. In addition, the presence of terminal cyanide Fe(II)−C≡N− ligands, the number of which increases with the Fe^{II}/Fe^{III} ratio, is also possible. They can be randomly distributed through the surface in vicinity to K^+ ions where small fraction of Fe(III) ions can be reduced to Fe(II). This is consistent with other reports in the literature [85] where it is shown that in contrast to the bulk PBAs, the molecular PBAs may contain both bridged and terminal cyanide groups. In the later case, the nitrogen atoms of the terminal cyanide ligands can be utilized as a Lewis base or a hydrogen bond acceptor site to extend the structure. Thus, their presence is usually an indication that the PBAs are sensitive and response to chemical stimuli and extensions of the molecular structure. They are typically orientated in a trans position in respect to the plane of metal atoms.

Both K-NiFe-PBAs systems contain a small fraction of Fe(II) ions which concentrations vary depending on the potassium and Ni content. This was unambiguously proven by the Mössbauer data and showed that the reduction of some Fe(III) ions occurs (probably by CN species or autoreduction) in order to achieve a stable structure. It can be explained considering the reactions that may occur during the co-precipitation method. In the synthesis, $K_3Fe(CN)_6$ disassociates into K^+ and $[Fe^{III}(CN)_6]^{3-}$ ions in the acidic aqueous solution of $Ni(NO_3)_2.6H_2O$ (pH ~ 4). Thus, when Ni^{2+} ions are presented into the mixed solution, the residual $[Fe^{III}(CN)_6]^{3-}$ ions react with Ni^{2+} and K^+ ions, following Eq. (3):

$$Ni^{2+}_{(aq)} + \left[Fe^{III}(CN)_6\right]^{3-}_{(aq)} + 3K^{+}_{(aq)} + 2NO^{-}_{3(aq)} = KNi^{II}\left[Fe^{III}(CN)_6\right]\square\, nH_2O \ + 2K^{+}_{(aq)} + 2NO^{-}_{3(aq)} \tag{3}$$

However, potassium ions inserted into the $Ni^{II}[Fe^{III}(CN)_6]\ \square\ nH_2O$ structure may lead to a reduction of small fraction of Fe^{III} ions, to form the final product, according to Eq. (4):

$$KNi^{II}\left[Fe^{III}(CN)_6\right]\square\, nH_2O + K^{+}_{(aq)} + NO^{-}_{3(aq)} \leftrightarrow K_{x+y}Ni^{II}\left[Fe^{II}_{y}Fe^{III}_{1-y}(CN)_6\right]\square{\cdot}nH_2O\ (s) + NO^{-}_{3(aq)} \tag{4}$$

3.5.2. *H_2O–induced distortion of the framework of K-trace-NiFe-PBA upon adsorption at room temperature*

In an attempt to understand the effects induced by small changes in the pressure, a K-trace-NiFe-PBA sample (preliminary evacuated at 363 K) was contacted with water vapour (0.5 kPa equilibrium pressure) at ambient temperature for 20 min to reach equilibrium. Then, the spectra were acquired upon a decrease in the equilibrium pressure and evacuation upon vacuum treatment. The spectral changes occurring upon dehydration are illustrated in both Fig. 5A and B, showing the FTIR original and the difference spectra in the ν(C≡N) stretching region, respectively. The insets of the figure show the spectral changes in the ν(O−H) stretching (left) and δ(H_2O) deformation (right) regions.

As observed, the spectrum (a) of the hydrated material (0.5 kPa H_2O equilibrium pressure, Fig. 5A) is characterized with well–shaped and relatively narrow bands at 2168 and 2097 cm^{-1}. The gradual decrease in the H_2O pressure upon dehydration (spectra b–l) led to an overall broadening of the CN bands which appear with more developed high-frequency shoulders. It is known that the PBAs can interact with water molecules [86] through H–binding. Such interaction may influence the electronic density of the CN bonds and therefore, this sensitivity could modify the position of ν(C≡N) stretching bands. However, the analysis of the data presented in Fig. 5A shows the strengthening of only some of the CN bonds which is opposite to the expectations if they were affected by direct interaction with water. Thus, this indicates that the CN bonds became more heterogeneous which is a strong indication that the geometry of the framework has undergone slight structural distortion, as a consequence of the dehydration.

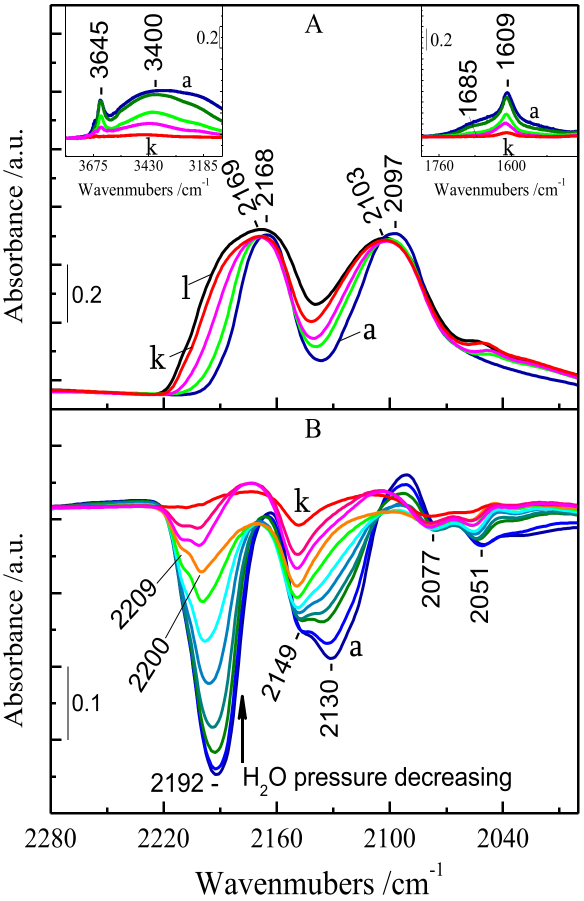

Fig. 5. FTIR original (A) and difference (B) spectra in the ν(C≡N) stretching region of adsorbed H_2O: equilibrium pressure of 0.5 kPa (spectrum a) and evolution of the spectra during evacuation at RT (spectra b – k) and at 363 K (spectrum l). The insets of the figure show the spectral changes in the ν(O−H) stretching (left) and δ(H_2O) deformation (right) regions.

To obtain more detailed information, we also analyzed the difference spectra presented in Fig. 5B. These spectra are produced by subtracting the original background spectra of the hydrated material and those upon evacuation at ambient temperature from that obtained after the sample was activated at 363 K. As it can be seen here, the adsorption leads to the development of a set of negative bands in the ν(C≡N) stretching region immediately after the introduction of 0.5 kPa H_2O to the system. Thus, at high water coverage, in the spectrum two strong bands with maxima at 2192, 2130, a shoulder at ~2149 cm^{-1}, and two weak features at 2077 and 2051 cm^{-1} are registered. The gradual decrease of the water vapor pressure (spectra b–k) leads to an overall progressive blue–shifts and attenuation of the intensities of the features until their almost complete disappearance. Finally, after prolonged evacuation, the initial spectrum of the activated sample (k) was almost fully restored. This indicates that most of the water molecules are weakly and reversibly adsorbed. The adsorption also gives rise to a couple of OH–stretching modes, presented in the spectra as a broad feature (the inset on the right) with a maximum at ca. 3400 cm^{-1} attributed to H–bonded hydroxyl groups.

The results demonstrate that the porous K-trace-NiFe-PBA framework sensitively responds to the water vapor pressure. The spectra show an overall red shift of the $\nu(C\equiv N)$ modes with an increasing the H_2O pressure. This behavior suggests that the lattice expands slightly, the framework space volume increases, thus affecting the M−CN bonds. The sensitivity of the $\nu(C\equiv N)$ stretching vibrations is consistent with previous studies [87,88] where it is shown that the bands in this fingerprint region can be used to determine the effect of the adsorption on the pore dimensions of different flexible cyanide–based MOFs. It should be noted, however, that in the latter case due to the flexibility of the ligands longer than the CN bonds, the structural changes are much more pronounced and the interaction with the guest molecules may cause phase transition.

A schematic illustration of the H_2O–induced expansion of the framework of KNi hexacyanoferrate PBA, consistent with our FTIR spectroscopic studies, is presented in Scheme 1. The process can be described to occur simultaneously by filling both the micro- and mesoporous channels of the material, and as a consequence, this results to expansion of the mesoporous structure.

PBAs are known [89] to behave as molecular sponges, exhibiting a strong affinity for water. The moisture sensitivity, however, could cause capacity fading during the CO_2 storage process. On the other hand, completely removing of water may introduce some extra complexity due to the structural rearrangements and alterations in the geometry of the framework. In particular, some studies based on single crystal X–ray structural analysis [90] show that removing coordinated water may results in octahedral – tetrahedral structural transformation. In addition, different PBAs have been reported to be sensitive to small structural distortions induced by external (mechanical) [47,48] or internal (chemical) pressure [49–51]. Although such slight distortions in PBAs in some cases are not easy detectable, a combination of different techniques based on X–ray [91], neutron diffraction [92] and X–ray magnetic circular dichroism [53] was used to understand and explain this behavior.

3.5.3. CO_2 adsorption at room temperature on hydrated/dehydrated K-NiFe-PBA

The porous NiFe-PBA framework containing minor amounts of alkali metals is highly sensitive to structural distortions induced by small changes under water vapor pressure. This sensitivity could affect the CO_2 adsorption. Therefore, additional studies of CO_2 adsorbed on K-trace-NiFe-PBA and K-rich-NiFe-PBA materials were also conducted. In these experiments, CO_2 (5 kPa) was adsorbed at ambient temperature and kept in contact with the sample for 20 min to reach an equilibrium. Then, the spectra are acquired upon a decrease in the equilibrium pressure and evacuation. The spectral changes are followed as a function of the decrease in CO_2 coverage in the samples pre-activated at 363 K. Similar experiments were also performed on the K-trace-NiFe-PBA sample pre-covered with 0.5 kPa H_2O at RT. Fig. 6A displays the FTIR spectra in the $\nu(CO_2)$ stretching region on both samples: under 5 kPa equilibrium pressure (spectrum a) and evolution of the spectra during decrease of the pressure (b–g) and evacuation (spectra h – j).

Adsorption of CO_2 (5 kPa equilibrium pressure) on dehydrated K-trace-NiFe-PBA initially leads to the development of a strong band in the $\nu(CO_2)$ region at 2338 cm^{-1} along with the respective “hot” band at ca. 2328 cm^{-1} and $^{13}CO_2$ feature registered as satellite of the principal band at ca. 2272 cm^{-1}. An overall blue shift of the band at 2338 cm^{-1} to 2340 cm^{-1} and a monotonic attenuation of the intensities of all features until their almost complete disappearance is observed with a gradual decrease in the CO_2 pressure (spectra b–j). These bands can be assigned based on former literature reports [17,93–96]. The most intense band detected at 2338 cm^{-1} at high coverages and its shift to a higher frequency with a decrease in pressure is assigned to the formation of weakly sorbed CO_2 species captured in the cavities of the framework. This indicates that the

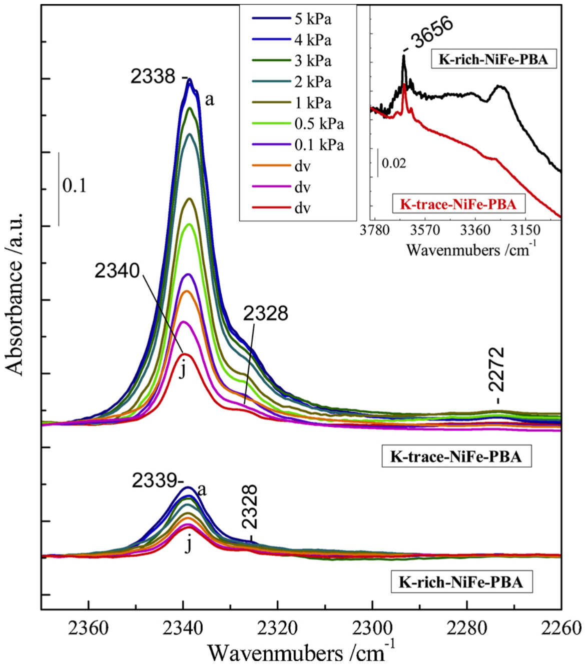

Fig. 6. Panel A. FTIR spectra in the $\nu(CO_2)$ stretching region of adsorbed CO_2 at ambient temperature – 5 kPa equilibrium pressure (spectrum a) and evolution of the spectra during decrease of the pressure (b–g) and evacuation (spectra h – j) on the dehydrated K-trace-NiFe-PBA and K-rich-NiFe-PBA. The inset shows the background spectra in the $\nu(OH)$ stretching region of the samples evacuated at 363 K before the CO_2 adsorption. The spectra are background and CO_2 gas–phase corrected.

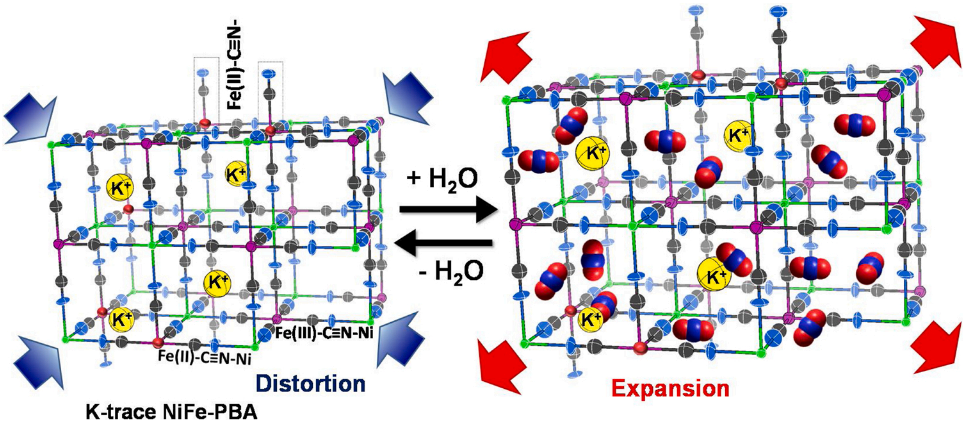

Scheme 1. Schematic illustration of the H_2O–induced expansion of the mesoporous structure of nickel hexacyanoferrate PBA with small amounts of K^+ ions.

intermolecular dispersion interaction may have significant contribution to the vibrational frequency shift in the porous materials and the CO_2 adsorption occurs mostly in the pores rather than on the external surface. In contrast to the K–trace-NiFe-PBA, the CO_2 adsorption on K-rich-Ni-Fe-PBA is much more suppressed and the bands corresponding to the CO_2 adsorbed species appeared with considerably reduced intensity. Moreover, the features after evacuation remained almost unaffected. The results are also in good agreement with the data described above in terms of the remarkable differences in the isosteric heats of adsorption and confirm that the presence of potassium in high concentrations leads to generation of highly basic sites strongly trapping CO_2. Thus, the process of regeneration of the adsorbent would require higher energy compared to that of K-trace-NiFe-PBA.

It should be noticed that CO_2 used in the adsorption experiments contains small amounts of water vapor which could be accumulated on the sample at the high CO_2 equilibrium pressures. Thus, similar to the sensitivity in the presence of water (as presented in Fig. 5), the ν(C≡N) characteristic bands were affected also by the CO_2 adsorption, particularly in the case of K-trace-NiFe-PBA. The process is accompanied by the appearance of a set of negative features in the ν(C≡N) stretching region at 2212, 2202, 2148, 2080, and 2058 cm^{-1} (shoulder) and several positive bands in the ν(OH) region (the inset of Fig. 6A), at 3698, 3663, 3603 cm^{-1}, and a broad feature at ca. 3443 cm^{-1} (Fig. S7, *Supplementary Information)*. However, comparing the intensities of the ν(C≡N) bands in Fig. S5, the results indicated that the water–induced expansion of the framework in this case is very negligible compared to that occurring under high H_2O vapor pressure (Fig. 5).

This suggests that pre–adsorbed water could affect/hinder the CO_2 uptake. Thus, we carried out a comparative study of CO_2 adsorption on almost fully dehydrated (evacuated at 363 K for 1 h) and hydrated K-trace-NiFe-PBA material (Fig. 7).

In order to minimize the effect of the presence of water vapor in the adsorbate, in these experiments, precisely controlled small doses of CO_2 equivalent to $\sim 5 \times 10^{-3}$ μmol each were successively introduced onto dehydrated (A) and water- pre-loaded sample (B) until an equilibrium pressure of 5 kPa CO_2 was reached in the IR cell. Analysis of the FTIR spectra presented in Fig. 7 reveals that the introduction of the first small doses of CO_2 in both cases leads to the appearance of the principal bands at 2338 cm^{-1} along with the respective “hot” band at 2328 cm^{-1}.

The CO_2 adsorption on the sample (A) when majority of the framework space volume is water–free (inset of Fig. 7) starts with the formation of physically adsorbed CO_2 species similar to the experiments preformed on almost fully hydrated material (B) without any significant differences. With further increase of the CO_2 doses, the features gradually increase in intensity. This behavior shows that H_2O hardly affects the CO_2 adsorption and these types of materials are perspective for CO_2 capture in the presence of water. It can also be suggested that the water–induced expansion of the framework may provide an additional space volume for accommodating CO_2 molecules and thus, to ensure certain conditions for CO_2 capture.

The host–guest interaction chemistry and dynamics of the K-NiFe-PBAs systems within CO_2 water and their adsorption behavior can be explained considering their different composition and porosity. In the case of K-trace-NiFe-PBA, the structure is composed of cavities between the contiguous nanoparticles, thus forming a system of mesoporous channels with larger dimensions compared to that of K-rich-NiFe-PBA. This suggests that the presence of higher number of $[Fe(CN)_6]^-$ vacancies generated in the absence of any significant amounts of interstitial K^+ cations plays a major role in the adsorption. The process can be described to occur simultaneously by filling both the micro- and mesoporous channels of the material. In the case of K-rich-NiFe-PBA, the presence of K^+ ions may contribute as active binding sites for trapping CO_2 stronger, however, the higher alkali content leads to pore blocking of the structure and capacity fading during the CO_2 storage process. These arguments are also supported by the analysis of the adsorption isotherms, the CO_2 storage capacity and the isosteric heat of CO_2 adsorption.

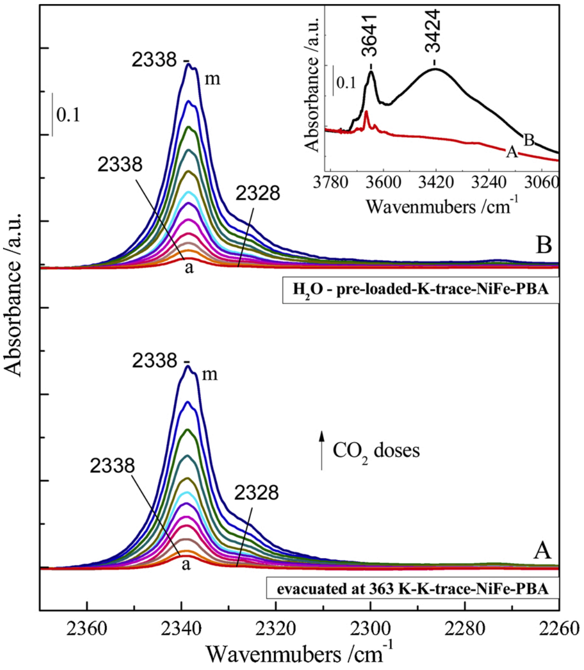

Fig. 7. FTIR spectra (a–l) in the $\nu(CO_2)$ stretching region of adsorbed CO_2 at ambient temperature on almost fully dehydrated (evacuated at 363 K for 1 h) (A) and hydrated K-trace-NiFe-PBA material (H_2O-pre-loaded) (B) after each precisely controlled small dose of CO_2 equivalent to $\sim 4.8 \times 10^{-3}$ μmol and the spectrum (m) at an equilibrium CO_2 pressure of 5 kPa. The inset shows the background spectra in the ν(OH) stretching region of the sample before the CO_2 adsorption. The spectra are background and CO_2 gas–phase corrected.

Due to the moisture sensitivity, the CO_2 adsorption can be affected by the overwhelming competitive adsorption of water molecules for identical adsorption sites. Thus, to obtain information on the presence of unsaturated metal centers, we performed FTIR analysis of low-temperature CO adsorption. Carbon monoxide is one of the most commonly used IR probe molecules and gives information on the existence and state of different surface acid and metallic sites [97]. We utilized the ^{13}CO and $^{13}C^{18}O$ isotopologues in order to shift down the carbonyl frequencies and to avoid the hindrance from the overlapping contributions of the CN stretching vibrations. The experiments were performed on the K-trace-NiFe-PBA pre-activated at 363 K.

As presented in Fig. S8, in both cases the adsorption does not lead to the appearance of any intense carbonyl bands, *i.e.* the amount of the accessible unsaturated metal ions is low. A careful inspection of the spectra reveals that the band at 2054 cm^{-1} disappeared and a new band broader at 2024 cm^{-1} was formed instead. Because the bands position are not isotope sensitive, we attribute this phenomenon to a CO-induced shift of the cyanide band at 2054 cm^{-1} to 2024 cm^{-1}. In addition to this, it can be seen that the adsorption of ^{13}CO (panel A, spectrum a) leads to the appearance of a low-intensity shoulder at around 2130 cm^{-1}. The feature shifted to ~2071 cm^{-1} when $^{13}C^{18}O$ (Panel B, spectrum a,) was adsorbed and the isotopic shift factor was consistent with the theoretically calculated one [98]. These two bands correspond to a $^{12}C^{16}O$ carbonyl band at 2171 cm^{-1}. The spectral changes during the adsorption can be clearly seen in the insets of Fig. S8, where the background corrected spectra after each small dose of carbon monoxide and the spectrum (a) at an equilibrium pressure of 0.5 kPa are presented. According to summarized literature data [97], the bands at 2130 cm^{-1} (^{13}CO) and at 2071 cm^{-1} ($^{13}C^{18}O$) could be assigned to Fe^{2+}-CO or Ni^{2+}-CO species. It should be underlined that the respective metal sites are connected with the CN species responsible for the appearance of the cyanide band at 2054 cm^{-1}. In conclusion, the CO adsorption proceeds through the formation of a small amount of carbonyl species. However, the amount of the Lewis acid sites is negligible and their existence has very minor effect and do not play a crucial role in the adsorption of CO_2 and H_2O.

4. Conclusions

Two different K-containing nickel hexacyanoferrate Prussian Blue Analogues (K-NiFe-PBAs) with a cubic crystal structure were synthesized *via* a co–precipitation method. The composition analysis *via* EDX–SEM reveals that the as-synthesized compounds are characterized with substantially different Ni:K atomic ratios of ca. 2.5 and 12 and composition containing rich– or trace amounts of potassium due to the charge balance. The FTIR spectroscopy studies reveal the presence of two main coordination units of Fe(III)−CN−Ni(II) and Fe(II)−CN−Ni(II) building the structure. The Mössbauer spectroscopy also shows that the changes in the composition by increasing the Ni:K ratio reflects mostly in a noticeable decrease of the fraction of Fe(II) at the expense of Fe(III) ions. The structure of both as-synthesized K-NiFe-PBAs, of nominal composition $K_{x+y}Ni^{II}[Fe^{II}{}_{y}Fe^{III}{}_{1-y}(CN)_6]$ □ $n\cdot H_2O$ can be described including $Ni(NC)_6$ and $M(CN)_6$ entities ($M{=}Fe^{III}$, Fe^{II}) that are linked by sharing of cyanide bridging groups and forming a three-dimensional cubic framework of linearly repeating –NC–M–CN–Ni–NC units. In addition, the presence of terminal cyanide Fe(II)−C≡N− ligands, the number of which increases with the Fe^{II}/Fe^{III} ratio, is also possible. They can be randomly distributed through the surface in vicinity to K^+ ions where small fraction of Fe(III) ions can be reduced to Fe(II). The porous nature of the materials is explained with the presence of $Fe(CN)_6]^{3-}$ vacancies, generated together with the interstitial cations to produce charge balance in the framework. The porosity of the K-NiFe-PBAs was found to correlate with the content of alkali K^+ ions inserted into the framework and it can readily be adjusted *via* charge balance. Thus, the number of the vacancies can be tuned by varying the Ni:K atomic ratio in the Prussian blue framework. In the case of K-trace-NiFe-PBA which has a more developed porous structure the number of the vacancies is considerably higher compared to that of K-rich-NiFe-PBA. The higher K content dictates the formation of a fully occupied cubic framework enclosing much smaller cavities. In contrast, with the K-trace-NiFe-PBA the alkali ions occupancy is much lower and this creates larger cavities in the framework.

The kinetics of N_2 adsorption and desorption is typical of materials with a mixed type micro– and mesoporous structure. The enhanced surface area and the pore size in K-trace-NiFe-PBA are attributed to more accessible channels obtained when the majority of the framework space volume is free of potassium cations.

The CO_2 adsorption isotherms clearly demonstrate that the synthesized K-trace-NiFe-PBA material offers an excellent alternative as an efficient adsorbent for CO_2 capture. The achieved CO_2 adsorption capacity of ca. 3.0 mmol g^{-1} CO_2 at 287 K and 100 kPa is comparable with other well–established CO_2 adsorbents. The isosteric heat of adsorption can easily be modulated and optimized *via* changing the Ni:K ratio thus, covering the thermodynamic criterion for capture and release of CO_2 with acceptable energy costs. Initially, at low CO_2 coverages, the heat released during the CO_2 storage on K-trace-NiFe-PBA is estimated to be significantly lower ($\sim$ 23.8 kJ mol^{-1}) compared to that of K-rich-NiFe-PBA ($\sim$ 56.2 kJ mol^{-1}), indicating that the presence of K^+ cations inserted in the PB framework may act synergistically to generate highly basic binding sites for trapping CO_2 stronger. The multilayer CO_2 adsorption leads to a gradual decrease of the host–guest interactions and the CO_2 adsorption at high coverages occurs mostly physically.

In situ FTIR spectroscopy was employed to elucidate the host–guest interaction chemistry and dynamics of K-NiFe-PBA systems within CO_2 and H_2O. The analysis of the vibrational ν(C≡N) modes indicates that the Prussian blue network containing trace amounts of K undergoes slight distortions upon H_2O adsorption. As a consequence, the lattice expands, leading to an increase of the framework space volume. The CO_2 adsorption when majority of the framework space volume is water–free starts with the formation of physically adsorbed CO_2 species similar to that on almost fully hydrated material without any significant differences. This behavior showed that H_2O hardly affects the CO_2 physisorption and these types of materials are perspective for CO_2 capture in the presence of water. In the case of K-trace-NiFe-PBA, the presence of higher number of $[Fe(CN)_6]^-$ vacancies generated in the absence of any significant amounts of interstitial K^+ cations play a major role in the adsorption. The process can be described to occur simultaneously by filling both the micro- and mesoporous channels of the material. On the other hands, in the case of K-rich-NiFe-PBA, the presence of K^+ ions may contribute as active binding sites for trapping CO_2 stronger, however, the higher alkali content leads to pore blocking of the structure and capacity fading during the CO_2 storage process. The amount of the Lewis acid sites is negligible and their existence has very minor effect and do not play a crucial role in the adsorption of CO_2 and H_2O.

Author statement

Stanislava Andonova: Conceptualization; Investigation; Writing- Original draft preparation; **Sina Sadigh Akbari:** Sample synthesis; Investigation; **Ferdi Karadaş:** Investigation; Writing- Reviewing and Editing; **Ivanka Spassova:** Investigation; **Daniela Paneva:** Investigation; **Konstantin Hadjiivanov:** Writing- Reviewing and Editing.

Declaration of Competing Interest

The authors report no declarations of interest.

Acknowledgments

This work was supported by the Bulgarian Ministry of Education and Science (Contract No. DO1-214/28.11.2018) under the National Research Programme "Low-carbon Energy for the Transport and Domestic Use - EPLUS" approved by DCM #577/17.08.2018. S.S.A. thanks TUBITAK for support (Project No: 118Z277).

Appendix A. Supplementary data

Supplementary material related to this article can be found, in the online version, at doi:https://doi.org/10.1016/j.jcou.2021.101593.

References

[1] J. Goldemberg, Ethanol for a sustainable energy future, Science 315 (2007) 808–810, https://doi.org/10.1126/science.1137013.

[2] N.B. Grimm, S.H. Faeth, N.E. Golubewski, C.L. Redman, J. Wu, X. Bai, J.M. Briggis, Global change and the ecology of cities, Science 319 (2008) 756–760, https://doi.org/10.1126/science.1150195.

[3] M.M. Maroto-Valer, C. Song, Y. Soong (Eds.), Environmental Challenges and Greenhouse Gas Control for Fossil Fuel Utilization in the 21st Century, Springer, US, 2002. New York, ISBN 978-1-4615-0773-0774.

[4] J.D. Figueroa, T. Fout, S. Plasynski, H. McIlvried, R.D. Srivastava, Advances in CO_2 capture technology-The U.S. Department of Energy's Carbon Sequestration Program, Int. J. Greenh. Gas Control 2 (2008) 9–20, https://doi.org/10.1016/S1750-5836(07)00094-1.

[5] J. Wang, L. Huang, R. Yang, Zh. Zhang, J. Wu, Y. Gao, Q. Wang, D. O'Hare, Z. Zhong, Recent advances in solid sorbents for CO_2 capture and new development trends, Energy Environ. Sci. 7 (2014) 3478–3518, https://doi.org/10.1039/C4EE01647E.

[6] J. Shang, G. Li, R. Singh, Q. Gu, K.M. Nairn, T.J. Bastow, N. Medhekar, C. M. Doherty, A.J. Hill, J.Z. Liu, P.A. Webley, Discriminative separation of gases by a "Molecular Trapdoor" mechanism in chabazite zeolites, J. Am. Chem. Soc. 134 (2012) 19246–19253, https://doi.org/10.1021/ja309274y.

[7] T.D. Pham, Q. Liu, R.F. Lobo, Carbon dioxide and nitrogen adsorption on cation-exchanged SSZ-13 zeolites, Langmuir 29 (2013) 832–839, https://doi.org/10.1021/la304138z.

[8] S. Kumar, R. Srivastava, J. Koh, Utilization of zeolites as CO_2 capturing agents: advances and future perspectives, J. CO2 Util. 41 (2020), 101251, https://doi.org/10.1016/j.jcou.2020.101251.

[9] Y. Li, X. Wang, M. Cao, Three-dimensional porous carbon frameworks derived from mangosteen peel waste as promising materials for CO_2 capture and super capacitors, J. CO2 Util. 27 (2018) 204–216, https://doi.org/10.1016/j.jcou.2018.07.019.

[10] A.E. Creamer, B. Gao, Carbon-based adsorbents for post combustion CO_2 capture: a critical review, Environ. Sci. Technol. 50 (2016) 7276–7289, https://doi.org/10.1021/acs.est.6b00627.

[11] J. Yu, M. Guo, F. Muhammad, A. Wang, F. Zhang, Q. Li, G. Zhu, One-pot synthesis of highly ordered nitrogen-containing mesoporous carbon with resorcinol–urea–formaldehyde resin for CO_2 capture, Carbon 69 (2014) 502–514, https://doi.org/10.1016/j.carbon.2013.12.058.

[12] G. Singh, J. Lee, A. Karakoti, R. Bahadur, J. Yi, D. Zhao, K. AlBahily, A. Vinu, Emerging trends in porous materials for CO_2 capture and conversion, Chem. Soc. Rev. 49 (2020) 4360–4404, https://doi.org/10.1039/D0CS00075B.

[13] J. Yu, Y. Le, B. Cheng, Fabrication and CO_2 adsorption performance of bimodal porous silica hollow spheres with amine-modified surfaces, RSC Adv. 2 (2012) 6784–6791, https://doi.org/10.1039/C2RA21017G.

[14] P. Zhao, G. Zhang, Y. Xu, Y. Lv, Amine functionalized hierarchical bimodal mesoporous silicas as a promising nanocomposite for highly efficient CO_2 capture, J. CO2 Util. 34 (2019) 543–557, https://doi.org/10.1016/j.jcou.2019.08.001.

[15] J. Yu, L.-H. Xie, J.-R. Li, Y. Ma, J.M. Seminario, P.B. Balbuena, CO_2 capture and separations using MOFs: computational and experimental studies, Chem. Rev. 117 (2017) 9674–9754, https://doi.org/10.1021/acs.chemrev.6b00626.

[16] R. Aniruddha, I. Sreedhar, B.M. Reddy, MOFs in carbon capture-past, present and future, J. CO2 Util. 42 (2020), 101297, https://doi.org/10.1016/j.jcou.2020.101297.

[17] K.I. Hadjiivanov, D.A. Panayotov, M.Y. Mihaylov, E.Z. Ivanova, K.K. Chakarova, S. M. Andonova, N.L. Drenchev, Power of infrared and raman spectroscopies to characterize metal-organic frameworks and investigate their interaction with guest molecules, Chem. Rev. 121 (2021) 1286–1424, https://doi.org/10.1021/acs.chemrev.0c00487.

[18] M. Mihaylov, K. Chakarova, S. Andonova, N. Drenchev, E. Ivanova, A. S. Sabetghadam, J. Gascon, F. Kapteijn, K. Hadjiivanov, Adsorption forms of CO_2 on MIL-53(Al) and NH_2-MIL-53(Al) as revealed by FTIR spectroscopy, J. Phys. Chem. C 120 (2016) 23584–23595, https://doi.org/10.1021/acs.jpcc.6b07492.

[19] M. Mihaylov, K. Chakarova, S. Andonova, N. Drenchev, E. Ivanova, E.A. Pidko, A. S. Sabetghadam, J. Gascon, F. Kapteijn, K. Hadjiivanov, Adsorption of CO_2 on MIL-53(Al): FTIR evidence of the formation of dimeric CO_2 species, Chem. Commun. 52 (2016) 1494–1497, https://doi.org/10.1039/C5CC08677A.

[20] M. Mihaylov, S. Andonova, K. Chakarova, A. Vimont, E. Ivanova, N. Drenchev, K. Hadjiivanov, An advanced approach for measuring acidity of hydroxyls in confined space: a FTIR study of low-temperature CO and $^{15}N_2$ adsorption on MOF samples from the MIL-53(Al) series, Phys. Chem. Chem. Phys. 17 (2015) 24304–24314, https://doi.org/10.1039/C5CP04139B.

[21] N.L. Drenchev, K.K. Chakarova, O.V. Lagunov, M.Y. Mihaylov, E.Z. Ivanova, I. Strauss, K.I. Hadjiivanov, In situ FTIR spectroscopy as a tool for investigation of gas/solid interaction: water-enhanced CO_2 adsorption in UiO-66 metal-organic framework, J. Vis. Exp. 15 (2020), e60285, https://doi.org/10.3791/60285.

[22] S. Andonova, E. Ivanova, J. Yang, K. Hadjiivanov, Adsorption forms of CO_2 on MIL-53(Al) and MIL-53(Al)–OH_x as revealed by FTIR spectroscopy, J. Phys. Chem. C 121 (2017) 18665–18673, https://doi.org/10.1021/acs.jpcc.7b05538.

[23] E. Deniz, F. Karadaş, H.A. Patel, S. Aparicio, C.T. Yavuz, M. Atilhan, A combined computational and experimental study of high pressure and supercritical CO_2 adsorption on Basolite MOFs, Microporous Mesoporous Mater. 175 (2013) 34–42, https://doi.org/10.1016/j.micromeso.2013.03.015.

[24] Y. Jung, F. Karadaş, S. Zulfiqar, E. Deniz, S. Aparicio, M. Atilhan, C.T. Yavuz, S. M. Han, Limitations and high pressure behavior of MOF-5 for CO_2 capture, Phys. Chem. Chem. Phys. 15 (2013) 14319–14327, https://doi.org/10.1039/C3CP51768C.

[25] W.-J. Li, Ch. Han, G. Cheng, Sh.-L. Chou, H.-K. Liu, Sh.-X. Dou, Chemical Properties, Structural properties, and energy storage applications of Prussian Blue Analogues, Small 15 (2019), 1900470, https://doi.org/10.1002/smll.201900470.

[26] J. Estelrich, M.A. Busquets, Prussian Blue: a safe pigment with zeolitic-like activity, Int. J. Mol. Sci. 22 (2021) 780–794, https://doi.org/10.3390/ijms22020780.

[27] L. Han, X.Y. Yu, X.W. Lou, Formation of Prussian-Blue-Analog nanocages via a direct etching method and their conversion into Ni–Co-mixed oxide for enhanced oxygen evolution, Adv. Mater. 28 (2016) 4601, https://doi.org/10.1002/adma.201506315.

[28] Y. You, X.L. Wu, Y.X. Yin, Y.G. Guo, High-quality Prussian blue crystals as superior cathode materials for room-temperature sodium-ion batteries, Energy Environ. Sci. 7 (2014) 1643, https://doi.org/10.1039/C3EE44004D.

[29] S. Liu, G.L. Pan, G.R. Li, X.P. Gao, Copper hexacyanoferrate nanoparticles as cathode material for aqueous Al-ion batteries, J. Mater. Chem. A 3 (2015) 959–962, https://doi.org/10.1039/C4TA04644G.

[30] S.S. Kaye, J.R. Long, Hydrogen storage in the dehydrated Prussian Blue Analogues $M_3[Co(CN)_6]_2$ (M = Mn, Fe, Co, Ni, Cu, Zn), J. Am. Chem. Soc. 127 (2005) 6506–6507, https://doi.org/10.1021/ja051168t.

[31] C.P. Krap, J. Balmaseda, L.F. del Castillo, B. Zamora, E. Reguera, Hydrogen storage in Prussian Blue Analogues: H_2 interaction with the metal found at the cavity surface, Energy Fuels 24 (2010) 581–589, https://doi.org/10.1021/ef900823s.

[32] A. Ould-Hamouda, A. Iazzolino, H. Tokoro, Sh.-ichi Ohkoshi, E. Freysz, Large optical third-order nonlinearities in a switchable Prussian blue analogue, Optical Mater. Express 7 (2017) 444–453, https://doi.org/10.1364/OME.7.000444.

[33] H. Tokoroa, Shin-ichi Ohkoshi, Novel magnetic functionalities of Prussian blue analogs, Dalton Trans. 40 (2011) 6825–6833, https://doi.org/10.1039/C0DT01829E.

[34] G. Fornasieri, A. Bordage, A. Bleuzen, Magnetism and photomagnetism of Prussian Blue Analogue nanoparticles embedded in porous metal oxide ordered nanostructures, Eur. J. Inorg. Chem. 3–4 (2018) 259–271, https://doi.org/10.1002/ejic.201700819.

[35] T.G.U. Ghobadi, A. Ghobadi, M. Buyuktemiz, E.A. Yildiz, D.B. Yildiz, H. G. Yaglioglu, Y. Dede, E. Ozbay, F. Karadaş, A. Robust, Precious-metal-free dye-sensitized photoanode for water oxidation: a nanosecond-long excited-state lifetime through a Prussian Blue Analogue, Angew. Chem. Int. Ed. 59 (2020) 4082–4090, https://doi.org/10.1002/anie.201914743.

[36] M. Aksoy, S.V.K. Nune, F. Karadaş, A Novel synthetic route for the preparation of an amorphous Co/Fe Prussian Blue Coordination compound with high electrocatalytic water oxidation activity, Inorg. Chem. 55 (2016) 4301–4307, https://doi.org/10.1021/acs.inorgchem.6b00032.

[37] E.P. Alsaç, S.V.K. Nune, E. Ülker, Y. Dede, F. Karadaş, Tuning the electronic properties of Prussian Blue Analogues for efficient water oxidation electrocatalysis: experimental and computational studies, Chem. Eur. J. 24 (2018) 4856–4863, https://doi.org/10.1002/chem.201704933.

[38] G.U. Ghobadi, A. Ghobadi, M.C. Soydan, M.B. Vishlaghi, S. Kaya, E. Ozbay, F. Karadaş, Strong light–matter interactions in Au plasmonic nanoantennas coupled with Prussian Blue Catalyst on BiVO4 for photoelectrochemical water splitting, ChemSusChem. 13 (2020) 2577–2588, https://doi.org/10.1002/cssc.202000294.

[39] F. Karadaş, H. El-Faki, E. Deniz, C.T. Yavuz, S. Aparicio, M. Atilhan, CO_2 adsorption studies on Prussian blue analogues, Microporous Mesoporous Mater. 162 (2012) 91–97, https://doi.org/10.1016/j.micromeso.2012.06.019.

[40] P.K. Thallapally, R.K. Motkuri, C.A. Fernández, B.P. McGrail, G.S. Behrooz, Prussian Blue Analogues for CO_2 and SO_2 capture and separation applications, Inorg. Chem. 49 (2010) 4909–4915, https://doi.org/10.1021/ic902397w.

[41] S. Natesakhawat, J.T. Culp, Ch. Matranga, B. Bockrath, Adsorption properties of hydrogen and carbon dioxide in Prussian Blue Analogues $M_3[Co(CN)_6]_2$, m = Co, Zn, J. Phys. Chem. C 111 (2007) 1055–1060, https://doi.org/10.1021/jp065845x.

[42] R.K. Motkuri, P.K. Thallapally, B.P. McGrail, S.B. Ghorishi, Dehydrated Prussian blues for CO_2 storage and separation applications, Cryst. Eng. Comm. 2 (2010) 4003–4006, https://doi.org/10.1039/C0CE00199F.

[43] D.O. Ojwang, J. Grins, G. Svensson, The adsorption kinetics of CO_2 on copper hexacyanoferrate studied by thermogravimetric analysis, Microporous Mesoporous Mater. 272 (2018) 70–78, https://doi.org/10.1016/j.micromeso.2018.06.019.

[44] G. Svensson, J. Grins, D. Eklöf, L. Eriksson, D. Wardecki, C. Thoral, L. Bodoignet, Influence of the presence of ifferent alkali cations and the amount of $Fe(CN)_6$ vacancies on CO_2 adsorption on copper hexacyanoferrates, Materials 12 (2019) 3371–3383, https://doi.org/10.3390/ma12203371.

[45] R. Roque-Malherbe, F. Lugo, R. Polanco, Synthesis, structural elucidation and carbon dioxide adsorption on Zn (II) hexacyanoferrate (II) Prussian blue analogue, Appl. Surf. Sci. 385 (2016) 360–367, https://doi.org/10.1016/j.apsusc.2016.04.139.

[46] R. Roque-Malherbe, E. Carballo, R. Polanco, F. Lugo, C. Lozano, Structure and adsorption properties of a porous cooper hexacyanoferrate polymorph, J. Phys. Chem. Solids 86 (2015) 65–73, https://doi.org/10.1016/j.jpcs.2015.04.009.

[47] M. Ohba, W. Kaneko, S. Kitagawa, T. Maeda, M. Mito, Pressure response of three-dimensional cyanide-bridged bimetallic magnets, J. Am. Chem. Soc. 130 (2008) 4475–4484, https://doi.org/10.1021/ja7110509.

[48] A. Bleuzen, J.-D. Cafun, A. Bachschmidt, M. Verdaguer, P. Münsch, F. Baudelet, J.-P. Itié, CoFe Prussian Blue Analogues under variable pressure. Evidence of departure from cubic symmetry: X-ray diffraction and absorption study, J. Phys. Chem. C 112 (2008) 17709–17715, https://doi.org/10.1021/jp805852n.

[49] J.E. Auckett, A.A. Barkhordarian, S.H. Ogilvie, S.G. Duyker, H. Chevreau, V. K. Peterso, C.J. Kepert, Continuous negative-to-positive tuning of thermal expansion achieved by controlled gas sorption in porous coordination frameworks, Nat. Commun. 9 (2018), 4873, https://doi.org/10.1038/s41467-018-06850-6.

[50] B. Xie, L. Wang, J. Shu, X. Zhou, Zh. Yu, H. Huo, Y. Ma, X. Cheng, G. Yin, P. Zuo, Understanding the structural evolution and lattice water movement for rhombohedral Nickel hexacyanoferrate upon sodium migration, ACS Appl. Mater. Interfaces 11 (2019) 46705–46713, https://doi.org/10.1021/acsami.9b15073.

[51] A.L. Goodwin, K.W. Chapman, C.J. Kepert, Guest-Dependent negative thermal expansion in nanoporous Prussian Blue Analogues $M^{II}Pt^{IV}(CN)_6\cdot x\{H_2O\}$ $(0 \le x \le 2$; m = Zn, Cd), J. Am. Chem. Soc. 127 (2005) 17980–17981, https://doi.org/10.1021/ja056460f.

[52] A. Bordage, L. Nataf, F. Baudelet, A. Bleuzen, Investigation of prussian blue analogs by XMCD at the K-edge of transition metals, J. Phys.: Conf. Ser. 712 (2016), 012109, https://doi.org/10.1088/1742-6596/712/1/012109.

[53] J.-D. Cafun, J. Lejeune, J.-P. Itié, F. Baudelet, A. Bleuzen, XMCD at the transition metal K-edges as a probe of small pressure-induced structural distortions in Prussian Blue Analogues, J. Phys. Chem. C 117 (2013) 19645–19655, https://doi.org/10.1021/jp403337w.

[54] Q. Gao, J. Chen, Q. Sun, D. Chang, Q. Huang, H. Wu, A. Sanson, R. Milazzo, H. Zhu, Q. Li, Zh. Liu, J. Deng, X. Xing, Switching between giant positive and negative thermal expansions of a $YFe(CN)_6$ -based Prussian Blue Analogue induced by guest species, Angew. Chem. Int. Ed. 56 (2017) 9023–9028, https://doi.org/10.1002/anie.201702955.

[55] B.C. Lippens, J.H. de Boer, Studies on pore systems in catalysts: V. The t method, J. Catal. 4 (1965) 319–323, https://doi.org/10.1016/0021-9517(65)90307-6.

[56] C.D. Wessells, R.A. Huggins, Y. Cui, Copper hexacyanoferrate battery electrodes with long cycle life and high power, Nat. Commun. 2 (2011) 550, https://doi.org/10.1038/ncomms1563.

[57] D. Zhao, Y. Lu, D. Ma, Effects of structure and constituent of Prussian Blue Analogs on their application in oxygen evolution reaction, Molecules 25 (2020) 2304, https://doi.org/10.3390/molecules25102304.

[58] W. Zhang, Y. Zhao, V. Malgras, Q. Ji, D. Jiang, R. Qi, K. Ariga, Y. Yamauchi, J. Liu, J.-S. Jiang, M. Hu, Synthesis of monocrystalline nanoframes of Prussian Blue

Analogues by controlled preferential etching, Angew. Chem. Int. Ed. 55 (2016) 8228–8234, https://doi.org/10.1002/anie.201600661.

[59] X. Su, Y. Wang, J. Zhou, S. Gu, J. Li, Sh. Zhang, Operando spectroscopic identification of active sites in NiFe Prussian Blue Analogues as electrocatalysts: activation of oxygen atoms for oxygen evolution reaction, J. Am. Chem. Soc. 140 (2018) 11286–11292, https://doi.org/10.1021/jacs.8b05294.

[60] Q. Niu, C. Bao, X. Cao, Ch. Liu, H. Wang, W. Lu, Ni–Fe PBA hollow nanocubes as efficient electrode materials for highly sensitive detection of guanine and hydrogen peroxide in human whole saliva, Biosens. Bioelectron. 141 (2019), 111445, https://doi.org/10.1016/j.bios.2019.111445.

[61] K.S.W. Sing, D.H. Everett, R.A.W. Haul, L. Moscou, R.A. Pieroti, J. Rouquerol, T. Siemieniewska, Reporting physisorption data for gas/solid systems with special reference to the determination of surface area and porosity, Pure Appl. Chem. 57 (1985) 603–619, https://doi.org/10.1351/pac198557040603.

[62] Y. Yue, A.J. Binder, B. Guo, Z. Zhang, Z.-A. Qiao, C. Tian, S. Dai, Mesoporous Prussian Blue Analogues: template-free synthesis and sodium-ion battery applications, Angew. Chem. Int. Ed. 53 (2014) 3134–3137, https://doi.org/10.1002/anie.20131067.

[63] L. Hu, P. Zhang, Q.-wang Chen, Ji-yang Mei, N. Yan, Room-temperature synthesis of Prussian blue analogue $Co_3[Co(CN)_6]_2$ porous nanostructures and their CO_2 storage properties, RSC Adv. 1 (2011) 1574–1578, https://doi.org/10.1039/C1RA00624J.

[64] A. Jaffe, J.R. Long, Ordered absences out of the blue, Nature 578 (2020) 222–223, https://doi.org/10.1038/d41586-020-00329-5.

[65] A. Simonov, T. De Baerdemaeker, H.L.B. Boström, M.L.R. Gómez, H.J. Gray, D. Chernyshov, A. Bosak, H.-B. Bürgi, A.L. Goodwin, Hidden diversity of vacancy networks in Prussian blue analogues, Nature 578 (2020) 256–260, https://doi.org/10.1038/s41586-020-1980-y.

[66] D.O. Ojwang, J. Grins, D. Wardecki, M. Valvo, V. Renman, L. Häggström, T. Ericsson, T. Gustafsson, A. Mahmoud, R.P. Hermann, G. Svensson, Structure, characterization and properties of K-containing copper hexacyanoferrate, Inorg. Chem. 55 (2016) 5924–5934, https://doi.org/10.1021/acs.inorgchem.6b00227.

[67] A.S. Abouelwafa, A. Hauser, V. Mereacre, Y. Lan, G.J. Long, F. Grandjean, G. Buth, Ch.E. Anson, A.K. Powell, Search for electron delocalization from $[Fe(CN)_6]^{3-}$ to the dication of viologen in $(DNP)_3[Fe(CN)_6]_2\cdot 10H_2O$, Inorg. Chem. 56 (2017) 6477–6488, https://doi.org/10.1021/acs.inorgchem.7b00540.

[68] C.W. Ng, J. Ding, L.M. Gan, Microstructural changes induced by thermal treatment of Cobalt(II) hexacyanoferrate(III) compound, J. Solid State Chem. 156 (2001) 400–407, https://doi.org/10.1006/jssc.2000.9013.

[69] S. Cavenati, C.A. Grande, E. Rodrigues, Adsorption Equilibrium of Methane, Carbon dioxide, and nitrogen on Zeolite 13X at high pressures, Chem. Eng. Data 49 (2004) 1095–1101, https://doi.org/10.1021/je0498917.

[70] Z. Zhang, M. Xu, H. Wang, Z. Li, Enhancement of CO_2 adsorption on high surface area activated carbon modified by N_2, H_2 and ammonia, Chem. Eng. J. 160 (2010) 571–577, https://doi.org/10.1016/j.cej.2010.03.070.

[71] Z. Zhang, S. Huang, S. Xian, H. Xi, Z. Li, Adsorption equilibrium and kinetics of CO_2 on chromium terephthalate MIL-101, Energy Fuels 25 (2011) 835–842, https://doi.org/10.1021/ef101548g.

[72] Z. Zhao, Z. Li, Y.S. Lin, Adsorption and diffusion of carbon dioxide on Metal−Organic Framework (MOF-5), Ind. Eng. Chem. Res. 48 (2009) 10015–10020, https://doi.org/10.1021/ie900665f.

[73] M. Ding, R.W. Flaig, H.-L. Jiang, O.M. Yaghi, Carbon capture and conversion using metal–organic frameworks and MOF-based materials, Chem. Soc. Rev. 48 (2019) 2783–2828, https://doi.org/10.1039/C8CS00829A.

[74] N. Li, Z. Chang, H. Huang, R. Feng, W.-W. He, M. Zhong, D.G. Madden, M. J. Zaworotko, X.-He Bu, Specific K^+ binding sites as CO_2 traps in a porous MOF for enhanced CO_2 selective orption, Small 15 (2019), 1900426, https://doi.org/10.1002/smll.201970118.

[75] J. Lejeune, J.-B. Brubach, P. Roy, A. Bleuzen, Application of the infrared spectroscopy to the structural study of Prussian blue analogues, Compt. Rend. Chim. 17 (2014) 534–540, https://doi.org/10.1016/j.crci.2014.01.017.

[76] C.W. Ng, J. Ding, Y. Shi, L.M. Gan, Structure and magnetic properties of copper(II) hexacyanoferrate(III) compound, J. Phys. Chem. Solids 62 (2001) 767–775, https://doi.org/10.1016/S0022-3697(00)00248-1.

[77] S.A. Agnihotry, P. Singh, A.G. Joshi, D.P. Singh, K.N. Sood, S.M. Shivaprasad, Electrodeposited Prussian blue films: annealing effect, Electrochim. Acta 51 (2006) 4291–4301, https://doi.org/10.1016/j.electacta.2005.12.008.

[78] O. Sato, Y. Einaga, A. Fujishima, K. Hashimoto, Photoinduced long-range magnetic ordering of a Cobalt−Iron cyanide, Inorg. Chem. 38 (1999) 4405–4412, https://doi.org/10.1021/ic980741p.

[79] Y. Zhao, B. Liang, X. Wei, K. Li, C. Lv, Y. Zhao, A core–shell heterostructured CuFe@NiFe Prussian blue analogue as a novel electrode material for high-capacity and stable capacitive deionization, J. Mater. Chem. A 7 (2019) 10464–10474, https://doi.org/10.1039/C8TA12433G.

[80] Zi-Y. Yu, Y. Duan, J.-D. Liu, Y. Chen, X.-K. Liu, W. Liu, T. Ma, Y. Li, X.-S. Zheng, T. Yao, M.-R. Gao, J.-F. Zhu, B.-J. Ye, S.-H. Yu, Unconventional CN vacancies suppress iron-leaching in Prussian blue analogue pre-catalyst for boosted oxygen evolution catalysis, Nat. Commun. 10 (2019) 2799, https://doi.org/10.1038/s41467-019-10698-9.

[81] J. Li, L. He, J. Jiang, Z. Xu, M. Liu, X. Liu, H. Tong, Z. Liu, D. Qian, Facile syntheses of bimetallic Prussian blue analogues ($K_xM[Fe(CN)_6]\cdot nH_2O$, M=Ni, Co, and Mn) for electrochemical determination of toxic 2-nitrophenol, Electrochim. Acta 353 (2020), 136579, https://doi.org/10.1016/j.electacta.2020.136579.

[82] K.I. Hadjiivanov, Identification of neutral and charged N_xO_y surface species by IR spectroscopy, Catal. Rev. 42 (2000) 71–144, https://doi.org/10.1081/CR-100100260.

[83] In: I. Bresinska, R.S. Drago, P.A. Jacobs (eds.), Zeolite Chemistry and Catalysis, 1991, ISBN: 9780080887227.

[84] H. Niwa, T. Moriya, T. Shibata, Y. Fukuzumi, Y. Moritomo, In situ IR spectroscopy during oxidation process of cobalt Prussian blue analogues, Sci. Rep. 11 (2021) 4119, https://doi.org/10.1038/s41598-021-83699-8.

[85] M. Nihei, Molecular Prussian Blue Analogues: from bulk to molecules and low-dimensional aggregates, Chem. Lett. 49 (2020) 1206–1215, https://doi.org/10.1246/cl.200428.

[86] K.W. Chapman, P.D. Southon, C.L. Weeks, C.J. Kepert, Reversible hydrogen gas uptake in nanoporous Prussian Blue analogues, Chem. Commun. (2005) 3322–3324, https://doi.org/10.1039/B502850G.

[87] G. Kumari, K. Jayaramulu, T.K. Maji, C. Narayana, Temperature induced structural transformations and gas adsorption in the Zeolitic Imidazolate Framework ZIF-8: a Raman study, J. Phys. Chem. A 117 (2013) 11006–11012, https://doi.org/10.1021/jp407792a.

[88] M. Shao, M.-X. Li, Z.-X. Wang, X. He, H.-H. Zhang, Structural diversity and vibrational spectra of nine Cu(I)-cyanide metal–organic frameworks with in situ generated N-heterocyclic ligands, Cryst. Growth Des. 17 (2017) 6281–6290, https://doi.org/10.1021/acs.cgd.7b00967.

[89] C. Duan, Y. Meng, Y. Wang, Z. Zhang, Y. Ge, X. Li, Y. Guo, D. Xiao, High-crystallinity and high-rate Prussian Blue analogues synthesized at the oil–water interface, Inorg. Chem. Front. 8 (2021) 2008–2016, https://doi.org/10.1039/D0QI01361G.

[90] H. Ohmagari, R. Ohtani, M. Nakaya, M. Ohba, M. Nakamura, L.F. Lindoy, O. Satod, S. Hayami, Water-dependent charge-transfer-induced spin transition of Prussian blue analogues, Dalton Trans. 45 (2016) 16784–16788, https://doi.org/10.1039/C6DT03474H.

[91] S. Margadonna, K. Prassides, A.N. Fitch, Zero thermal expansion in a Prussian Blue Analogue, J. Am. Chem. Soc. 126 (2004) 15390–15391, https://doi.org/10.1021/ja044959o.

[92] D.M. Pajerowski, V.O. Garlea, E.S. Knowles, M.J. Andrus, M.F. Dumont, Y.M. Calm, S.E. Nagler, X. Tong, D.R. Talham, M.W. Meisel, Magnetic neutron scattering of thermally quenched K-Co-Fe Prussian blue analog photomagnet, Phys. Rev. B 86 (2012), 054431, https://doi.org/10.1103/PhysRevB.86.054431.

[93] P.D.C. Dietzel, R.E. Johnsen, H. Fjellvag, S. Bordiga, E. Groppo, S. Chavan, R. Blom, R. Adsorption properties and structure of CO_2 adsorbed on open coordination sites of metal–organic framework Ni2(dhtp) from gas adsorption, IR spectroscopy and X-ray diffraction, Chem. Commun. 44 (2008) 5125–5127, https://doi.org/10.1039/B810574J.

[94] L. Valenzano, J.G. Vitillo, S. Chavan, B. Civalleri, F. Bonino, S. Bordiga, C. Lamberti, Structure–activity relationships of simple molecules adsorbed on CPO-27-Ni metal–organic framework: In situ experiments vs. theory, Catal. Today 182 (2012) 67–79, https://doi.org/10.1016/j.cattod.2011.07.020.

[95] S.R. Miller, G.M. Pearce, P.A. Wright, F. Bonino, S. Chavan, S. Bordiga, I. Margiolaki, N. Guillou, G. Feŕey, S. Bourrelly, Structural transformations and adsorption of fuel-related gases of a structurally responsive Nickel Phosphonate Metal−Organic Framework, Ni-STA-12, J. Am. Chem. Soc. 130 (2008) 15967–15981, https://doi.org/10.1021/ja804936z.

[96] K. Tan, S. Zuluaga, Q. Gong, Y. Gao, N. Nijem, J. Li, T. Thonhauser, Y.J. Chabal, Competitive coadsorption of CO_2 with H_2O, NH_3, SO_2, NO, NO_2, N_2, O_2, and CH_4 in M-MOF-74 (M = Mg, Co, Ni): the role of hydrogen bonding, Chem. Mater. 27 (2015) 2203–2217, https://doi.org/10.1021/acs.chemmater.5b00315.

[97] K.I. Hadjiivanov, G.N. Vayssilov, Characterization of oxide surfaces and zeolites by carbon monoxide as an IR probe molecule, Adv. Catal. 47 (2002) 307–511, https://doi.org/10.1016/S0360-0564(02)47008-3.

[98] K. Hadjiivanov, M. Mihaylov, D. Panayotov, E. Ivanova, K. Chakarova, Isotopes in the FTIR investigations of solid surfaces, Spectrosc. Prop. Inorg. Organomet. Compd. 45 (2014) 43–78, https://doi.org/10.1039/9781782621485-00043.